High-Resolution ISAR Imaging With Sparse Stepped-Frequency Waveforms

Lei Zhang, Zhi-jun Qiao, *Member, IEEE*, Mengdao Xing, *Member, IEEE*, Yachao Li, and Zheng Bao, *Senior Member, IEEE*

***Abstract*—From the theory of compressive sensing (CS), we know that the exact recovery of an unknown sparse signal can be achieved from limited measurements by solving a sparsity-constrained optimization problem. For inverse synthetic aperture radar (ISAR) imaging, the backscattering field of a target is usually composed of contributions by a very limited amount of strong scattering centers, the number of which is much smaller than that of pixels in the image plane. In this paper, a novel framework for ISAR imaging is proposed through sparse stepped-frequency waveforms (SSFWs). By using the framework, the measurements, only at some portions of frequency subbands, are used to reconstruct full-resolution images by exploiting sparsity. This waveform strategy greatly reduces the amount of data and acquisition time and improves the antijamming capability. A new algorithm, named the sparsity-driven High-Resolution Range Profile (HRRP) synthesizer, is presented in this paper to overcome the error phase due to motion usually degrading the HHRP synthesis. The sparsity-driven HRRP synthesizer is robust to noise. The main novelty of the proposed ISAR imaging framework is twofold: 1) dividing the motion compensation into three steps and therefore allowing for very accurate estimation and 2) both sparsity and signal-to-noise ratio are enhanced dramatically by coherent integrant in cross-range before performing HRRP synthesis. Both simulated and real measured data are used to test the robustness of the ISAR imaging framework with SSFWs. Experimental results show that the framework is capable of precise reconstruction of ISAR images and effective suppression of both phase error and noise.**

***Index Terms*—Compressive sensing (CS), inverse synthetic aperture radar (SAR) (ISAR), radar imaging, sparse stepped-frequency waveform (SFW) (SSFW).**

I. Introduction

MODERN INVERSE synthetic aperture radar (SAR) (ISAR) is a wonderful tool for target identification and classification and has robust performance under all-weather circumstances and the ability of interference suppression. Therefore, ISAR imaging could be utilized in many military and civilian applications including moving-target recognition, aircraft traffic control, and air/space surveillance. For these ISAR applications, high resolution is usually essential to characterize target features. Conventionally, the cross-range resolution of an ISAR image is obtained from the diversity of the radar-viewing angle to the target and high down-range resolution is achieved by increasing the system bandwidth. Stepped-frequency waveforms (SFWs) are able to use the wide radio-frequency (RF) band of a frequency-agile radar with a narrowband receiver. Therefore, SFWs have been widely employed to increase system bandwidth and achieve high-resolution range profiles (HRRPs) of targets. In the ISAR systems associated with SFW, high down-range resolution is handled from a series of short monotonic and continuous pulses transmitted with a fixed pulse repetition frequency (PRF), where each pulse is equipped with a frequency-modulated (FM) signal. A sequence of FM pulses, stepped in frequency by a fixed amount, is called a burst. High range resolution is achieved by coherently synthesizing subpulses of a burst into a single wideband signal, and therefore, here, we do not require the wide instantaneous bandwidth [1], [2]. The enhancement of range resolution from SFWs provides better performance of imaging and feature extraction [3]–[5]. Thus, SFWs can be applied to furnish imaging capability as well as improving performance for the narrowband radar systems. However, SFW ISARs are sensitive to phase errors and several significant error sources can corrupt the phase coherence of subpulses, including radial motion inducing phase change, atmospheric effects, and hardware instabilities. To compensate phase error for high-resolution image generation, some approaches have been proposed recently [6]–[8].

The ISAR with SFW yields wide synthetic bandwidth at the cost of longer observing time and has a normally shorter functional range (due to the high PRF) than that of a conventional wideband radar. The high PRF is usually applied in ISAR with SFW to get enough coherent bursts, but it generates range ambiguity for farther target returns and has a limitation in detection range due to the short pulse duration for accumulation gain. In the cases of low and median PRFs, the ISAR with SFW suffers from very long observing time. However, the multifunctional radars often have other critical activities in addition to imaging, such as searching and target tracking. As a result, observing time for each target is usually limited. Furthermore, in a long observing interval, both target oscillations and radial motions of ISAR with SFW can seriously distort the coherence of subpulses and thus degrade the performance of profile synthesis processing. Another fragile aspect of the conventional SFW radar is its sensitivity to interference. In real situations, radars often encounter strong interference, such as RF interference, self-induced interference, artificial interference, etc. [9], [10]. Therefore, some portions of subpulses of a

Manuscript received May 30, 2010; revised October 25, 2010 and January 16, 2011; accepted May 1, 2011. This work was supported by the "973" Program of China under Grant 2010CB731903. The work of Z. Qiao was supported in part by the U.S. Army Research Office under Contract/Grant W911NF-08-1-0511 and in part by the Texas Norman Hackerman Advanced Research Program under Grant 003599-0001-2009.

L. Zhang, M. Xing, Y. Li, and Z. Bao are with the National Key Laboratory of Radar Signal Processing, Xidian University, Xi'an 710071, China (e-mail: zhanglei_0330@126.com; xmd@xidian.edu.cn; bzh@xidian.edu.cn).

Z. Qiao is with the Department of Mathematics, The University of Texas-Pan American, Edinburg, TX 78539-2999 USA (e-mail: qiao@utpa.edu).

Color versions of one or more of the figures in this paper are available online at http://ieeexplore.ieee.org.

Digital Object Identifier 10.1109/TGRS.2011.2151865

burst may be unusable due to these interferences. Consequently, it can be quite difficult to generate well-focused imagery even if most subpulses of the burst are clean. To alleviate the constraints imposed on ISAR with SWF during the observing time and sensitivity to interference, a natural extension is to employ the so-called sparse SFWs [11]. Radar systems with sparse SFWs are as simple as the conventional SF radar but have some significant advantages. Obviously, in a sparse SFW radar, a burst would have less subpulses due to the vacancy in frequency bands. As a result, the observing interval for collecting burst signal is proportionally short and also improves coherence of subpulses. Interference sources can be directly overcome in sparse SFW radars by avoiding the interference frequency bands. So, sparse SFW radars can operate in dense electromagnetic environments. These superiorities make sparse SFWs a novel technique for modern radar applications. In the procedure for using sparse SFWs, some essential elements should be taken into account. First, we need a sparse SFW synthesizer for HRRP and an approach for the corresponding phase-error compensation. Conventional SF synthesis methods are based on Fourier transforms. If we directly apply them to sparse SFWs processing, the presence of high sidelobes and grating lobes causes a dramatic degradation of image quality. In order to reduce sidelobes and grating lobes caused by missing frequency bands, some new algorithms have been proposed. In [11], the sequence CLEAN (S-CLEAN) approach was successfully applied to form a high-resolution image with sparse frequency waveforms. The bandwidth extrapolation technique leads a linear prediction model to extrapolate the band vacancy coherently while the spectral estimation technique is used to estimate model coefficients [12]. Super spatially variant apodization is another alternative approach to reconstruct a full-band spectrum using part of frequency samples. It has proven to be effective in sparse aperture filling [13] and resolution enhancement for high-resolution SAR imaging [14]. However, direct application of these methods to fulfill the sparse subbands encounters difficulties from both noise and model errors. In the range profile synthesis of sparse SFWs, phase error from target motion and other sources is inevitable but difficult to overcome. In general, the high quality of an ISAR image relies on the 2-D coherent accumulation to provide a high signal-to-noise ratio (SNR). Moreover, SNR gain is proportional to the amount of the signal accumulated. Because spare SFWs provide much less measurements than full frequency-band waveforms do, the image, generated by sparse SFWs, may be with low SNR and sharpness. As a result, a significant aspect in radar imaging with sparse SFWs is to overcome the image blurring and strong noise. This should be carefully taken into account.

ISAR imagery demonstrates the locations and amplitudes of strong scattering centers for a target scattering electric field in the range–Doppler (RD) plane, which represents the reflectivity of the target. Dominant scattering centers usually take up only a fraction of the whole bins of the RD plane, while signals from weak scattering centers contribute little to image formation. In this sense, the ISAR image is spatially sparse. Sparsity of an image can be exploited to achieve superresolution, denoising, and feature extraction [15]. In particular, the theory of compressive sensing (CS) or compressed sampling tells us that an unknown sparse signal can be exactly recovered from a very limited number of measurements with high probability by solving a convex l_1 optimization problem [16]–[18]. In the context of radar signal processing, CS has recently attracted much attention since one can obtain better performance and easier data acquisition and storage schemes. In [19], a CS-based ISAR imaging algorithm is proposed to estimate locations of scattering centers from very limited measurements, and in [20], the algorithm is improved by the weighted l_1 optimization. For a SAR image, the recovery with an optimized graph-structured dictionary is used to estimate the migratory scattering in wide-angle imaging [21]. In [22], a novel data acquisition and imaging method are presented for stepped-frequency continuous-wave ground-penetrating radars by exploiting spatial sparsity of strong targets underground. CS also has been successfully utilized in 3-D SAR reconstruction [23], [24]. All these works suggest to us that exploiting sparsity is a novel and very helpful tool in radar imaging. In the case of ISAR imaging with sparse SFWs, which is studied in this paper, the major difficulty is that the reconstruction of a high-resolution image is an ill-posed problem with mathematical uncertainty involved due to portions of missing frequency bands and model errors. In this paper, we propose a new framework for ISAR imaging with sparse SFWs by exploiting the intrinsic sparsity of target backscattering field.

The main features of our framework are as follows.

1) The sparsity of an ISAR signal in RD domain is used to construct a penalty function to recover synthetic HRRP with sparse SFWs. It can be also applied to the conventional SFWs.
2) It counts for all kinds of phase errors for HRRP synthesis without constrictions on phase formation.
3) It allows high-quality ISAR imaging with sparse SFWs under low SNR conditions.
4) A new scheme for the motion estimation is proposed to ensure accurate translational motion compensation.
5) The computational load is relatively high. We use conjugate gradient (CG) and fast Fourier transform (FFT) implementation to accelerate the estimation of phase error. However, it is still more time-consuming compared with conventional SFWs processing based on FFT. We may need a deeper study for the real-time implementation.

The organization of this paper is as follows. Section II introduces the received-signal model of sparse SFW and its HRRP synthesis by exploiting signal sparsity. In Section III, a novel compensation method is proposed to handle model errors and parameter selection, and in Section IV, we deal with ISAR imaging. Experimental results to data processing, both real and simulated, are given in Section V to show the effectiveness of the proposed approach.

II. Sparse SFW and HRRP Synthesis

A. Sparse SFW and Signal Model

A general SFW consists of a sequence of N narrowband pulses with carrier frequencies that increase from pulse to pulse. The carrier frequencies are indicated with $f_n = f_0 + n \cdot \Delta f$,

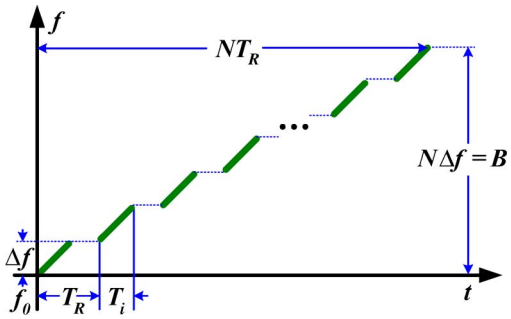

Fig. 1. Time–frequency profile of a burst for full-band SFW.

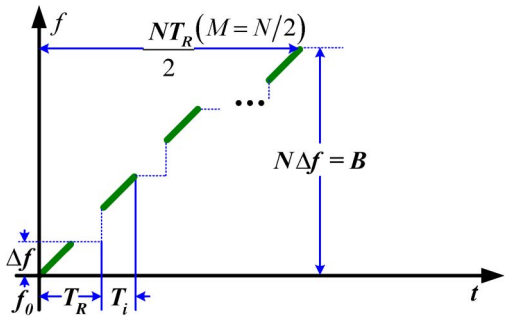

Fig. 2. Time–frequency profile of a burst for a sparse SFW (with only half subpulses of the full band waveform).

where $n = 0, 1, \ldots N-1$, f_0 is the fundamental carrier frequency, and Δf is the bandwidth of subpulse and usually equals the frequency step in the case of full-band SFW, so that N is the number of transmitted frequencies. Therefore, the analytic transmitted signal is

$$s_T(t) = \sum_{n=0}^{N-1} x(t - nT_R) \exp\left[j2\pi \cdot f_n \cdot (t - nT_R)\right] \quad (1)$$

where $x(t)$ is the complex envelope of the narrowband transmitted pulse and T_R is the pulse repetition interval. The total time length of the SFW is $(N-1)T_R + T_i$, where T_i is the pulse duration of a transmitted subpulse. The time interval $N \cdot T_R$ represents the coherent processing interval (CPI) required to synthesize an HRRP. The modulation form of $x(t)$ can be a simple rectangular pulse or a linear FM (LFM) pulse signal. Without loss of generality, we use the LFM waveform

$$x(t) = rect\left(\frac{t}{T_i}\right) \cdot \exp(j\pi\gamma t^2) \quad (2)$$

where the chirp rate is $\gamma = \Delta f / T_i$ and, thus, the bandwidth of a subpulse equals the frequency step. Fig. 1 shows the time–frequency characteristics of a full-band LFM-SFW in a burst, and B stands for the synthetic bandwidth. A sparse SFW can be directly expanded from the full-band SFW: If only portions of the full-band subpulses are transmitted, a sparse SFW is obtained. For example, by transmitting a subpulse every second for a burst such as Fig. 2 shows, we have $N/2$ (N is assumed as an even integer) subpulses in a burst, and this equally halves the processing interval required (from $N \cdot T_R$ to $(N \cdot T_R)/2$). In sparse SFWs, only a subset of frequency bands is measured and the subset can also be selected evenly or randomly from a full-band SFW burst. To make notations clear, the carrier frequencies of a spare SFW are denoted by $f_{sm} = f_0 + \boldsymbol{G}(m) \cdot \Delta f$, where $\boldsymbol{G}$ is a subset of $[0 : N-1]$ with $|\boldsymbol{G}| = M$ and m runs from 1 to M and represents the frequency sparse degree of the SFW. Then, a sparse SFW can be expressed in the following form:

$$s_{sT}(t) = \sum_{m=0}^{M-1} x(t - mT_R) \exp\left[j2\pi f_{sm}(t - mT_R)\right]. \quad (3)$$

The degree of a sparse SFW is defined by

$$\alpha = \frac{M \cdot \Delta f}{B} \quad (4)$$

where B is the synthesis bandwidth of the sparse SFW. Obviously, the generation of a sparse SFW is as simple as that of the conventional SFW for a radar system. Therefore, it is very easy to furnish the high-resolution imaging ability to some active radar systems operating with narrow bandwidth waveforms, with only nominal modifications. In addition, a sparse SFW has shorter time for data acquisition than conventional SFW radars. Another advantage is that the sparse SFW is capable of significantly reducing frequency interference of external RF sources. With the prior information of interferences, a sparse SFW radar system would be programmed to skip over the frequency bands with interferences so that clean and high SNR signals can be received.

Assuming that a target is composed of K dominant scattering centers with complex backscattering coefficients a_k, $k = 0, 1, \ldots K-1$, then the signal is given by

$$\begin{aligned} s(t) &= \sum_{k=0}^{K-1} a_k \cdot s_{sT}\left[t - \tau_k(t)\right] + n(t) \\ &= \sum_{k=0}^{K-1} a_k \sum_{m=0}^{M-1} x\left[t - \tau_k(t) - mT_R\right] \\ &\quad \cdot \exp\left\{j2\pi f_{sm} \cdot \left[t - \tau_k(t) - mT_R\right]\right\} + n(t) \end{aligned} \quad (5)$$

where $\tau_k(t) = 2R_k(t)/c$ stands for the time delay of the kth scattering center and $n(t)$ is the additive noise. Suppose that the time delay makes a weak change within a subpulse. After applying the "stop-and-go" model and imposing $\tau_k(t) \approx \tau_k(mT_R)$, where $\hat{t} = t - m \cdot T_R$, $\hat{t} \in [0, T_R]$, then the signal expression of the mth sweep can be rewritten as

$$\begin{aligned} S_m(\hat{t}) &= \sum_{k=0}^{K-1} a_k \cdot x\left[\hat{t} - \tau_k(mT_R)\right] \\ &\quad \cdot \exp\left\{j2\pi f_{sm} \cdot \left[\hat{t} - \tau_k(mT_R)\right]\right\} + n_m(\hat{t}) \end{aligned} \quad (6)$$

where $n_m(\hat{t})$ is the additive noise corresponding to the mth sweep. Therefore, the received signal of the mth sweep can be expressed in the frequency domain as follows:

$$\begin{aligned} s_m(\hat{f}) &= \sum_{k=0}^{K-1} a_k \cdot X(\hat{f}) \\ &\quad \cdot \exp\left\{-j2\pi \cdot \left[f_{sm} + \hat{f}\right] \cdot \tau_k(mT_R)\right\} + n_m(\hat{f}) \end{aligned} \quad (7)$$

where $\hat{f} \in [0, \Delta f]$ is the frequency corresponding to $\hat{t}$ and $X(\hat{f})$ is the Fourier transform of $x(\hat{t})$. By multiplying (7) by $X^*(\hat{f})$ ($*$ denotes conjugate) and ignoring some constants, we obtain the approximated expression for the mth subpulse in the range frequency domain, which is deduced by principle of stationary phase [25]. It is given by

$$\begin{aligned} sf_m(\hat{f}) &= \sum_{k=0}^{K-1} a_k \cdot rect\left(\frac{\hat{f}}{\Delta f}\right) \\ &\quad \cdot \exp\left\{-j2\pi \cdot [f_{sm} + \hat{f}] \cdot \tau_k(mT_R)\right\} + n_m(\hat{f}) \\ &= \sum_{k=0}^{K-1} a_k \cdot rect\left(\frac{\hat{f}}{\Delta f}\right) \\ &\quad \cdot \exp\left\{-j2\pi \cdot [f_{sm} + \hat{f}] \cdot \tau_k(0 \cdot T_R)\right\} \\ &\quad \cdot \exp\left[j \cdot (\delta_m + \phi_m)\right] + n_m(\hat{f}) \end{aligned} \tag{8}$$

where $\delta_m = -2\pi \hat{f} \cdot [\tau_k(mT_R) - \tau_k(0 \cdot T_R)]$ and $\phi_m = -2\pi f_{sm} \cdot [\tau_k(mT_R) - \tau_k(0 \cdot T_R)]$ denotes phase error for the mth subpulse. Both δ_m and ϕ_m degrade the performance of HRRP synthesis, but they have different meanings. δ_m stands for the range migration errors resulting from the scatters possibly moving out of a range cell during a burst acquisition time. For coherent radar systems, by using conventional methods for an SFW [6]–[8] or range profile alignment techniques [26]–[28], this error can be adjusted to an optimal degree so that the residual error is restricted within some proportions of a range cell. The quantity ϕ_m stands for the phase error among subpulses of a burst from target bulk motion, which is the major source degrading HRRP synthesis performance. Detailed analysis on ϕ_m can be found in [6]. In a later part of this paper, we will propose a new flow for the estimation of translational motion for echoes from sparse SFWs, which is anticipated to be accurate and robust to noise. The phase ϕ_m can be expended to include other phase errors, such as jitter of analog-to-digital converter, motion measurement inaccuracies, instabilities of the waveform generator, and some inherent approximations. In the SFW application, the major difficulty for generating the HRRP is how to compensate for ϕ_m. For simplicity, let us assume that δ_m is corrected ideally. Then, (8) can be rewritten as

$$\begin{aligned} sf_m(\hat{f}) &= \sum_{k=0}^{K-1} a_k \cdot rect\left(\frac{\hat{f}}{\Delta f}\right) \\ &\quad \cdot \exp\left\{-j2\pi \cdot [f_{sm} + \hat{f}] \cdot \tau_k(0 \cdot T_R)\right\} \\ &\quad \cdot \exp(j \cdot \phi_m) + n_m(\hat{f}). \end{aligned} \tag{9}$$

B. HRRP Synthesis by Exploiting Sparsity

In the case of full frequency-band SFWs, the reconstruction of the HRRP can be achieved by different techniques. There are two classical algorithms used for reconstructing a synthetic HRRP. One is where the range profile bins of all subpulses are sampled and then an inverse discrete Fourier transform (IDFT) is applied along the stepped frequency [6], and the other one involves arranging the subpulses in the frequency domain to obtain a wideband spectrum and then the HRRP is outputted after inverse FFT (IFFT). However, in the case of sparse SFWs, conventional methods for HRRP synthesis generate high sidelobes and grating lobes, which contaminate the HRRP dramatically and submerge real scattering centers. On the other hand, the theory of CS will enable us to reconstruct a sparse signal exactly from very limited measurements with high probability by solving a convex l_1 norm optimization problem [16]–[18]. The essence of CS lies in exploiting the sparsity of the objective signal by l_1 norm regularization. Before presenting the HRRP synthesis by exploiting sparsity, let us introduce the CS briefly. Let $\boldsymbol{y} \in \mathbf{C}^{\overline{L}}$ denote a finite signal of interest and a basis matrix $\boldsymbol{\Phi} = \{\boldsymbol{\varphi}_1, \boldsymbol{\varphi}_2, \ldots, \boldsymbol{\varphi}_L\}$ which satisfies $\boldsymbol{y} = \boldsymbol{\Phi}\boldsymbol{\theta}$, where $\boldsymbol{\theta}$ is a K-*sparse* vector (namely, it can be approximated by its K largest coefficients or its coefficients following a power decay law with K strongest coefficients [13]). One may reduce the measurement in the form of $\boldsymbol{s} = \mathbf{A}\boldsymbol{y}$ from N dimensions to M dimensions, where $\mathbf{A} \in \mathbf{C}^{\overline{L} \times L}$ ($\overline{L} < L$) is the measurement matrix satisfying $\boldsymbol{\Psi} = \mathbf{A}\boldsymbol{\Phi}$ (namely, the dictionary) and $\boldsymbol{\Psi}$ has the restricted isometry property (RIP) of order K [13]. Dictionary $\boldsymbol{\Psi}$ is required to satisfy K-RIP with a restricted isometry constant (RIC) $\delta_K \in (0, 1)$, which generally indicates that the optimal recovery of $\boldsymbol{y}$ can be done by the measurement $\overline{L} \geq O(K \cdot \log L)$. The K-order RIC of $\boldsymbol{\Psi}$ can be defined as the smallest quantity satisfying

$$(1 - \delta_K)\|\boldsymbol{\theta}\|_2^2 \leq \|\boldsymbol{\Psi}\boldsymbol{\theta}\|_2^2 \leq (1 + \delta_K)\|\boldsymbol{\theta}\|_2^2. \tag{10}$$

This property requires the dictionary's behavior to be like an isometry system on the K sparse signals. Each subset of K columns, extracted from $\boldsymbol{\Psi}$, is approximately orthogonal (but, exactly orthogonal is almost impossible since there are more columns than rows in $\boldsymbol{\Psi}$). It is not difficult for us to understand that the degree of orthogonality is represented by the RIC; a small RIC means strong orthogonality between any two columns and a RIC of 0.5 is usually an optimal choice for a stable CS performance. It is already proven that if $\overline{L} \geq O(K \cdot \log L)$, then the largest K coefficients can be estimated from $\boldsymbol{y}$ with overwhelming probability by solving a convex problem as

$$\min\left(\|\boldsymbol{\theta}\|_1\right), \text{ subject to } \|\boldsymbol{s} - \boldsymbol{F}\boldsymbol{\theta}\|_2 \leq \varepsilon \tag{11}$$

where $\|\cdot\|_p$ denotes l_p norm and $\min(\cdot)$ denotes the minimization and ε is the noise level. Clearly, some elements are specified in the CS: 1) a basis to support sparse representation of signal; 2) solver to the optimization problem; and 3) a measurement operator to provide considerable noncoherence among columns of the dictionary. In our case, i.e., ISAR imaging with a sparse SFW, in order to get strong incoherence of $\boldsymbol{\Psi}$, the waveform design should be accounted carefully, which we discuss in the following.

An HRRP determines the ranges and amplitudes of the strong centers of the target. Strong scattering centers usually take up

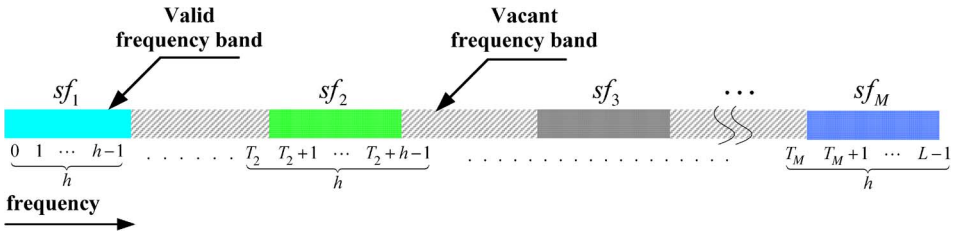

Fig. 3. Geometry of sparse SFM signal.

only a fraction of whole range bins, while signals from weak scattering centers contribute little to the HRRP formation. For our convenience, let us write the signal model of a sparse SFW burst of (7) in a compact vector form

$$\begin{aligned}\boldsymbol{s} &= \begin{bmatrix} sf_0 \\ sf_1 \\ \vdots \\ sf_m \\ \vdots \\ sf_{M-1} \end{bmatrix} = \mathbf{E}\cdot \begin{bmatrix} \mathbf{F}_0 \\ \mathbf{F}_1 \\ \vdots \\ \mathbf{F}_m \\ \vdots \\ \mathbf{F}_{M-1} \end{bmatrix} \cdot \boldsymbol{\theta} + \begin{bmatrix} n_0 \\ n_1 \\ \vdots \\ n_m \\ \vdots \\ n_{M-1} \end{bmatrix} \\ &= \mathbf{E}\cdot\mathbf{F}\cdot\boldsymbol{\theta} + \boldsymbol{n} \end{aligned} \tag{12}$$

where $\mathbf{E}$ is the diagonal matrix corresponding to phase error and $\mathbf{F} = \begin{bmatrix} \mathbf{F}_0 \\ \mathbf{F}_1 \\ \vdots \\ \mathbf{F}_m \\ \vdots \\ \mathbf{F}_{M-1} \end{bmatrix}$ is the partial Fourier matrix whose component $\mathbf{F}_m$ corresponds to the mth subpulse. They are presented in detail in the following. Hereafter, $\boldsymbol{\theta}$ is redefined as the complex HRRP that we want to recover. Let $\hat{f} = [0 : h-1]\cdot\Delta\hat{f}$ be the discrete form of the range frequency extent of a subpulse. Here, $\Delta\hat{f}$ is the frequency interval and the length of sf_m is assumed as h. Then, the size of frequency measurement vector $\boldsymbol{s}$ and noise $\boldsymbol{n}$ is $(\overline{L} = M\cdot h)\times 1$. And the length of HRRP $\boldsymbol{\theta}$ is assumed to be L. Then, the size of matrix $\mathbf{F}$ is $(M\cdot h)\times L$ and that of $\mathbf{E}$ is $(M\cdot h)\times(M\cdot h)$. In the application of sparse stepped-frequency-modulated (SFM) waveforms, we have $\overline{L} < L$. For clarity, we use Fig. 3 to show the geometry of a burst of the sparse SFM signal.

Suppose the frequency index of a full-band waveform is $[0 : L-1]$ and the mth subpulse consists of h frequency bins (whose index extent is from T_m to $T_m + h - 1$), where $0 \le T_m \le L - h$. In addition, we have

$$\mathbf{F}_m = \begin{bmatrix} 1 & \omega^{T_m} & \cdots & \omega^{(L-1)T_m} \\ 1 & \omega^{T_m+1} & \cdots & \omega^{(L-1)(T_m+1)} \\ \vdots & \vdots & \ddots & \vdots \\ 1 & \omega^{T_m+h-1} & \cdots & \omega^{(L-1)(T_m+h-1)} \end{bmatrix}_{T_m\times L}$$

$$\text{and}\quad \omega = \exp\left[-j\frac{2\pi}{L}\right]. \tag{13}$$

$\mathbf{F}_m$ is the partial Fourier matrix corresponding to the mth subpulse

$$\mathbf{E} = \mathbf{diag}\begin{bmatrix} \boldsymbol{e}_1 \\ \vdots \\ \boldsymbol{e}_m \\ \vdots \\ \boldsymbol{e}_M \end{bmatrix}_{\overline{L}\times\overline{L}} \tag{14}$$

where

$$\boldsymbol{e}_m = [\exp(j\cdot\phi_m), \exp(j\cdot\phi_m), \ldots, \exp(j\cdot\phi_m)]^{\mathrm{T}}_{1\times h} \tag{15}$$

corresponds to the phase error of the mth subpulse. Moreover, $[\cdot]^{\mathrm{T}}$ denotes the matrix transpose. Based on the signal model of (12), we develop the sparsity-driven HRRP synthesis in the next section. In this section, we develop the sparsity-driven HRRP synthesis based on Bayesian CS (BCS) [29] and neglect the phase error for simplicity. Generally, the components of $\boldsymbol{n}$ are approximated as a zero-mean complex Gaussian noise, namely, its imaginary and real parts (denoted by $\boldsymbol{n}_r$ and $\boldsymbol{n}_i$, respectively) are subject to an independent Gaussian distribution with unknown variance σ^2. The probability density function of $\boldsymbol{n}$ is given by

$$\begin{aligned} P(\boldsymbol{n}|\sigma^2) &= \left[(2\pi\sigma^2)^{-\frac{\overline{L}}{2}}\exp\left(-\frac{1}{2\sigma^2}\|\boldsymbol{n}_r\|_2^2\right)\right] \\ &\quad\cdot\left[(2\pi\sigma^2)^{-\frac{\overline{L}}{2}}\exp\left(-\frac{1}{2\sigma^2}\|\boldsymbol{n}_r\|_2^2\right)\right] \\ &= (2\pi\sigma^2)^{-\overline{L}}\exp\left(-\frac{1}{2\sigma^2}\|\boldsymbol{n}\|_2^2\right). \end{aligned} \tag{16}$$

According to BCS, the sparsity of $\boldsymbol{\theta}$ can be formulated by placing a sparseness-promoting prior on it. This sparseness prior is usually independently represented by a Laplace density function [29], which can be given by

$$P(\boldsymbol{\theta}|\gamma) = \left(\frac{\gamma}{2}\right)^{L}\exp\left(-\gamma\|\boldsymbol{\theta}\|_1\right) \tag{17}$$

where γ corresponds to the scale parameter of the Laplace distribution. Therefore, HRRP synthesis with SFWs is transferred into a classical problem to estimate $\boldsymbol{\theta}$ from noisy observation $\boldsymbol{s}$. For this purpose, the maximum *a posteriori* (MAP) estimator is used, which is given by

$$\hat{\boldsymbol{\theta}}(\boldsymbol{s}) = \arg\max_{\boldsymbol{\theta}\in\mathbf{C}_L}\left[P(\boldsymbol{\theta}|\boldsymbol{s})\right]. \tag{18}$$

Using the Bayes rule, we have

$$\hat{\boldsymbol{\theta}}(\boldsymbol{s}) = \arg\max_{\boldsymbol{\theta}\in\mathbf{C}_L} \left[P(\boldsymbol{s}|\sigma^2)\cdot P(\boldsymbol{\theta}|\gamma)\right]. \tag{19}$$

Clearly, (19) is also equivalent to

$$\hat{\boldsymbol{\theta}}(\boldsymbol{s}) = \arg\max_{\boldsymbol{\theta}\in\mathbf{C}_L} \left\{log\left[P(\boldsymbol{s}|\sigma^2)\right] + \log\left[P(\boldsymbol{\theta}|\gamma)\right]\right\}. \tag{20}$$

Substituting (16) and (17) into (20), the MAP estimator becomes

$$\begin{aligned}\hat{\boldsymbol{\theta}}(\boldsymbol{s}) &= \arg\max_{\boldsymbol{\theta}\in\mathbf{C}_L}\left\{-\frac{1}{2\sigma^2}\|\boldsymbol{s}-\mathbf{F}\boldsymbol{\theta}\|_2^2 - \gamma\|\boldsymbol{\theta}\|_1\right\}\\ &= \arg\min_{\boldsymbol{\theta}\in\mathbf{C}_L}\left\{\|\boldsymbol{s}-\mathbf{F}\boldsymbol{\theta}\|_2^2 + \lambda\|\boldsymbol{\theta}\|_1\right\}\end{aligned} \tag{21}$$

where $\lambda = 2\sigma^2\gamma$. In (21), the l_2 norm preserves the data fidelity of the solution and the l_1 norm minimizes most elements of $\boldsymbol{\theta}$ with a few large ones in accordance with the sparsity of HRRP. The optimization problem can be effectively solved by some algorithms and software [30], [31]. However, in practice, motion-induced range migration and phase error should be made up before the HRRP synthesis. In particular, the phase-error compensation is a significant task to be considered in the HRRP synthesis. A sparsity-driven HRRP synthesizer is proposed in this paper to jointly estimate phase error and reconstruct the HRRPs.

III. HRRP Synthesis and Phase-Error Compensation

A. Statistical Estimation for Noise and HRRP

In the issue of HRRP synthesis with a sparse SFW, the major difficulty is to compensate the phase error and accelerate the processing. Taking the phase error into account, we reformat the optimization problem in (21) as follows:

$$\hat{\boldsymbol{\theta}}(\boldsymbol{s}) = \arg\min_{\boldsymbol{\theta}\in\mathbf{C}_L}\left\{\|\boldsymbol{s}-\mathbf{E}\mathbf{F}\boldsymbol{\theta}\|_2^2 + \lambda\|\boldsymbol{\theta}\|_1\right\}. \tag{22}$$

Clearly, the sparsity coefficient λ is directly related to the statistics of both the noise and HRRP. For an optimal parameter λ, prior knowledge of noise and HRRP statistics is required. However, in practice, it is often unknown and should be estimated from data. In this sense, we convert the problem of selecting λ into obtaining the statistical information of noise and HRRP.

In radar signal processing, estimation of the noise statistics is available since Gaussian noise usually distributes evenly, and there are many range cells containing only noise. Given enough noise samples by those pure-noise cells, we can estimate σ^2 with high accuracy. Therefore, the problem to estimate noise variance is shifted to discriminating noise cells from cells containing signal components. Meanwhile, the scale parameter of the Laplace distribution placed on HRRP can be estimated from the signal bins. For sparse SFM waveforms, the noise samples can be extracted from the coarse range profiles generated by subpulses. The estimation of the statistical parameters of noise and HRRP contains the following three steps.

1) Coarse range profiles are generated by subpulses. Moreover, noncoherent summing is applied to them to generate high SNR range profiles.
2) Noise and target supports are separated by thresholds. Then, the noise and target samples are extracted from coarse range profiles.
3) Estimation of σ^2 and γ is performed by using the selected samples via maximum likelihood (ML) estimation. Moreover, parameter λ is obtained straightforwardly.

In step 1), we first generate coarse range profiles by IDFT. Generally, each subpulse provides enough frequency diversity to separate the scatters of a target into different range bins. Therefore, separating the bins containing the target signal from those with pure noise could be treated as a task of target detection with a wideband waveform. It is not difficult to understand that once we determine the range bins containing the noise only; the noise variance will be estimated approximately. Meanwhile, estimation of λ can be obtained from the target bins. Separating range cells containing the signal from those only containing noise is practicable by their energy difference, since signal energy is concentrated only on several range cells while noise distributes over all cells evenly after range compression. To enhance the SNR, we can sum up the amplitude of coarse range profiles incoherently in this step.

Step 2) is the detection process to separate noise and target in the summed range profile. Inspired by the ordered-statistics constant-false-alarm-rate (CFAR) detector [32], we can order range cells by their energy and determine the range cells with largest energy as signal cells and the rest as noise samples. With the prior knowledge of target size, the amount of range cells containing the signal (corresponding to detection order) could be determined approximately. In this paper, an energy-based threshold is proposed to perform a selection of noise samples adaptively. The upper threshold for the energy of range cells to select a noise cell is given as

$$Thres = E_m + \left[\sum_{l=1}^{h}\frac{(E_l - E_m)^2}{h-1}\right]^{\frac{1}{2}} \tag{23}$$

where E_l represents the energy of the lth range cell (there are h range cells for a coarse range profile) and E_m is the mean energy of all range cells of the summed range profile. When the energy of a range cell is below the threshold, it is determined as a pure-noise range bin. This energy-based threshold is composed by two terms: the energy mean and the square root of energy variance. Clearly, the threshold is adjusted with SNR adaptively: Given constant signal energy, in high SNR situations, we usually have relatively low threshold to maintain low false-alarm rate, whereas in low SNR situations, we get a high threshold, avoiding rejection of too many pure-noise range bins. For clarity, we give a detection result on the averaged coarse range profile of the Yak-42 data in Fig. 4, and the SNR is set as 10 dB. Clearly, the target support is discriminated from the noise bins effectively by using the adaptive threshold.

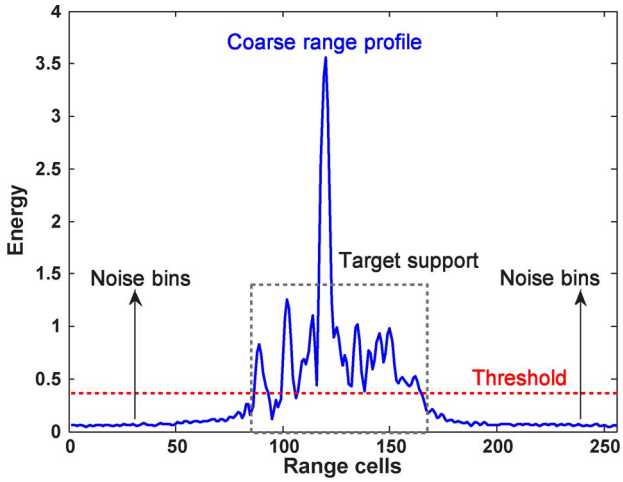

Fig. 4. Discrimination of target from noise in the coarse range profile.

By the energy-based threshold, we usually can extract a large number of noise bins from the summed range profile. Then, we need to determine the range bins containing dominant scattering centers. In order to do so, we use the CFAR detection to get the target bins. The CFAR threshold is given by

$$T_{\mathrm{CFAR}} = mean_n \cdot \eta \tag{24}$$

where $mean_n$ represents the amplitude mean of noise samples and η is a constant scale factor used to achieve a desired constant false-alarm probability under a given sample number. For an extensive mathematical study of a CFAR detector, [32] can be consulted. To calculate the constant scale factor, available software [33] can be used. Then, bins with amplitudes larger than the CFAR threshold are determined as strong scattering components, by which we reject some range bins with weak signals and noise from the target support. In the following experiments, the CFAR is set as 1%. Once the range bins containing the strong signal are discriminated from noise bins by the CFAR threshold, the support of strong signal in the range profile is determined. For our case of HRRP synthesis by exploiting sparse SFWs, we are usually interested in strong scattering centers only and define the ensemble of the indices of the strong scattering centers as the target support in the following statistical estimation. It should be emphasized that, in this step, we incoherently add the amplitude of all coarse range profiles to generate the coarse range profile with high SNR, and the noise and target detection is performed on it.

The task in the last step is to estimate σ^2 and γ from the separated noise and signal bins. Since we separate the noise and from target support in last step, we can extract range bins from the subband profiles corresponding to the noise indices as the pure-noise samples. In addition, the target range bins are determined by the detected target support corresponding to strong scattering centers. The ML estimate of σ^2 is the variance of all imagery and real parts of pure-noise bins (defined as $\hat{\sigma}^2$). Moreover, if we have the HRRP samples, we can estimate γ as the reciprocal of the amplitude mean of all HRRP bins, in accordance with the ML estimation. Herein, only having the subband range profiles in hand, we hence develop an estimator of γ as

$$\hat{\gamma} = \frac{1}{\frac{1}{L}\sum_{m=1}^{M}\sum_{l\in \boldsymbol{TS}}|pf_m(l)|} \tag{25}$$

where $\boldsymbol{TS}$ denotes the ensemble of the indices corresponding to the detected target support and pf_m stands for the coarse range profile corresponding to the mth subband. Finally, we have the sparsity coefficient as $\lambda = 2\hat{\sigma}^2\hat{\gamma}$.

B. HRRP Synthesis With Phase-Error Removal

After estimating the sparsity coefficient λ from the statistical parameters of both noise and HRRP, HRRP synthesis is performed by solving the optimization in (22). Generally, the strongest scattering centers contain the most essential information of the target. The next task is to solve the optimization in (22) efficiently. At first, in order to overcome the nondifferentiability of the l_1 norm around the origin, a useful approximation [15], [34]–[36] is employed by

$$\|\boldsymbol{\theta}\|_1 \approx \sum_{i=0}^{L-1}\left(|\boldsymbol{\theta}(i)|^2+\delta\right)^{\frac{1}{2}} \tag{26}$$

where $|\cdot|$ stands for the modulus operator and δ is a small nonnegative parameter. By introducing δ in (26), the nondifferentiability problem of $\|\boldsymbol{\theta}\|_1$ at the origin is overcome. Clearly, to ensure the approximation as rigid as possible, δ should be set small. Then, the optimization problem is reformatted as

$$\min\left(\|\boldsymbol{s}-\mathbf{EF}\boldsymbol{\theta}\|_2^2+\lambda\sum_{i=0}^{I-1}\left(|\boldsymbol{\theta}(i)|^2+\delta\right)^{\frac{1}{2}}\right). \tag{27}$$

In [35] and [36], it has been proven that the approximation of (26) keeps the correspondence between optimizations in (22) and (27) and the optimization in (27) also has a unique and exact solution. Furthermore, this solution tends to that of the optimization (22) as δ tends to zero. Therefore, if and only if a very small δ is used in (27), we will obtain a precise solution by solving (27) instead of (22). In our experiments, an experiential δ is 1×10^{-6} and other values, such as 0.001 and 0.01, also perform well, generating similar results. Therefore, the selection of δ should be small but with flexibility. A useful selection of δ is one in a thousand of the noise variance estimated from data so that it is small enough not to affect the behavior of the solution. Different from the problem given in (21), the phase error $\mathbf{E}$ in (27) is also unknown and should be estimated from measurement. Therefore, we need a new strategy for solving it. The quasi-Newton method with a specified Hessian update scheme is proven effective and efficient to solve the regularization optimization problem [15], [34]. For our topic of HRRP synthesis with phase error, a modified solver is presented in the following to estimate both HRRP and phase error simultaneously. Calculating the gradient of the objective function in (27), we have

$$\nabla(\boldsymbol{\theta}) = \hat{\mathbf{H}}(\boldsymbol{\theta})\boldsymbol{\theta} - 2\cdot\mathbf{F}^H\mathbf{E}^H\boldsymbol{s} \tag{28}$$

where the Hessian matrix is approximately equal to

$$\hat{\mathbf{H}}(\boldsymbol{\theta}) = 2\mathbf{F}^H\mathbf{E}^H\mathbf{E}\mathbf{F} + \lambda\mathbf{W}(\boldsymbol{\theta}) = 2\mathbf{F}^H\mathbf{F} + \lambda\mathbf{W}(\boldsymbol{\theta}) \quad (29)$$

and $\mathbf{W}(\boldsymbol{\theta})$ is a diagonal matrix

$$\mathbf{W}(\boldsymbol{\theta}) = \mathrm{diag}\left[\frac{1}{\left(|\boldsymbol{\theta}(0)|^2+\delta\right)^{1/2}}, \quad \frac{1}{\left(|\boldsymbol{\theta}(1)|^2+\delta\right)^{1/2}}, \quad \cdots \quad \frac{1}{\left(|\boldsymbol{\theta}(I-1)|^2+\delta\right)^{1/2}}\right]. \quad (30)$$

Apparently, the Hessian approximation relies on the objective variant $\boldsymbol{\theta}$. An iterative solution to (27) is determined through the following recursion formula:

$$\begin{aligned}\hat{\boldsymbol{\theta}}(g+1) &= 2\cdot\left[\hat{\mathbf{H}}\left(\hat{\boldsymbol{\theta}}(g)\right)\right]^{-1}\cdot\left[\mathbf{F}^H\left(\hat{\mathbf{E}}(g)\right)^H s\right] \\ &= \left[\mathbf{F}^H\mathbf{F}+\frac{\lambda}{2}\mathbf{W}\left(\hat{\boldsymbol{\theta}}(g)\right)\right]^{-1}\cdot\left[\mathbf{F}^H\left(\hat{\mathbf{E}}(g)\right)^H \boldsymbol{s}\right] \quad (31)\end{aligned}$$

where $\hat{\boldsymbol{\theta}}(g)$ and $\hat{\mathbf{E}}(g)$ are the estimations of $\boldsymbol{\theta}$ and $\mathbf{E}$, respectively, from the gth iteration. Without prior knowledge of the phase error corresponding to the mth subband, the initial value of iteration is $\hat{\phi}_m(0) = 0$, $m = 0, 1, \ldots, (M-1)$. The estimation of phase error $\hat{\phi}_m$ in the gth iteration is computed by

$$\exp\left[j\cdot\hat{\phi}_m(g+1)\right] = \exp\left[j\cdot\hat{\phi}_m(g)\right]\cdot\exp\left[j\cdot\Delta\hat{\phi}_m(g+1)\right] \quad (32)$$

where the updated exponential term is

$$\exp\left[j\cdot\Delta\hat{\phi}_m(g+1)\right] = \frac{\left(\hat{\boldsymbol{\theta}}(g+1)\right)^H\mathbf{F}_m^H\left(\hat{\mathbf{E}}_m(g)\right)^H sf_m}{\left|\left(\hat{\boldsymbol{\theta}}(g+1)\right)^H\mathbf{F}_m^H\left(\hat{\mathbf{E}}_m(g)\right)^H sf_m\right|}. \quad (33)$$

We increase g and go back to the iterative optimization problem (31) for the next iteration until $|\hat{\boldsymbol{\theta}}(g+1)-\hat{\boldsymbol{\theta}}(g)|_2/|\hat{\boldsymbol{\theta}}(g)|_2 \le \rho$, where ρ is a small parameter enough for the predetermined threshold or that g to reach a predetermined maximum iteration number. Generally, we set $\rho = 0.01$ or 0.001 while lower thresholds will not yield more precise solution but increase the computational load dramatically. The difference between the conventional phase-error correction and the current techniques for SFW in the formulation of HRRP synthesis with phase-error compensation is that no constraint is imposed on the form of phase errors. Therefore, our approach might be suitably applied in wide fields. Another feature of the proposed approach is its efficiency. Major computational load in each update sources from the matrix inversion calculation of $\hat{\mathbf{H}}(\hat{\boldsymbol{\theta}}(g))$ in (31). We note that the size of $\hat{\mathbf{H}}(\hat{\boldsymbol{\theta}}(g))$ is $L\times L$ and then the matrix inversion can be implemented with $L^3/3 + 2L^2 \approx L^3/3$ flops through a Cholesky factorization [37]. Moreover, we usually need several tens of updating iterations in (31) to reach an optimal convergence, making the proposed method low in efficiency. The CG algorithm [38] can be applied to accelerate the processing of matrix inversion calculation in (31). However, due to the iterative property of CG, its convergence may be slow as we need to perform the calculation of the linear system $\hat{\mathbf{H}}(\hat{\boldsymbol{\theta}}(g))\hat{\boldsymbol{\theta}}(g+1) = 2\cdot[\mathbf{F}^H(\hat{\mathbf{E}}(g))^H\boldsymbol{s}]$ over and over again in the gth update of (31). In order to improve the efficiency, we first analyze the properties of the Hessian matrix in (29). Its main characteristics are listed as follows.

1) Its size is $L\times L$.
2) It is symmetric positive definite.
3) The term $\mathbf{F}^H\mathbf{F}$ corresponds to the partial Fourier matrix, allowing us to use FFT to implement $\mathbf{F}^H\mathbf{F}\nu$ (ν denotes a $L\times 1$ vector) calculation efficiently. The FFT implementation of $\mathbf{F}^H\mathbf{F}\nu$ is very simple but effective. We perform the IFFT to ν and get ν_t and then set the components corresponding to the vacant frequency bands to zero and followed by an FFT. Therefore, taking only the multiple operations into account, $\mathbf{F}^H\mathbf{F}\nu$ can be implemented with about $L\log_2 L$ flops corresponding to two FFTs.
4) The term $\mathbf{W}$ is a diagonal matrix. We can use vector multiplication $w\odot\nu$ to evaluate matrix and vector multiplication $\mathbf{W}\nu$, where $w = [(1/(|\boldsymbol{\theta}(0)|^2+\delta)^{1/2}), (1/(|\boldsymbol{\theta}(1)|^2+\delta)^{1/2}), \ldots (1/(|\boldsymbol{\theta}(I-1)|^2+\delta)^{1/2})]^{\mathrm{T}}$ and $\odot$ denotes the Hadamard multiplication. As a result, $\mathbf{W}\nu$ is implemented by only L flops.

The main computational cost of the quasi-Newton solver to the sparsity-driven optimization lies in the following: 1) iterative update of (31) and 2) the CG solver to the linear system in each update of (31). For simplicity, we only account the multiple operations. For the number of the CG iterations to solve (31) being the N_{CG} case, the computation quantum of an FFT is $N_{\mathrm{CG}}L\log_2 L$ flops and that of the Hadamard multiplication is $N_{\mathrm{CG}}L$ flops. Therefore, the computational cost of CG in solving (31) is about $N_{\mathrm{CG}}L\log_2 L$ flops. Assuming that there are N_Q times of iterations in the quasi-Newton algorithm, the computation cost of the algorithm implemented by FFT-based CG is $N_QN_{\mathrm{CG}}L\log_2 L$ flops approximately, while the computational load of calculating matrix inversion through the Cholesky factorization is about $N_QL^3/3$ flops. Using the FFT-based CG can accelerate the convergence of the quasi-Newton solver effectively. For further improvement of efficiency, some optimization algorithms are available, such that the preconditioned CG algorithms [38], which could reduce the iteration number of conventional CG. In general, the computational complexity of the method is not a severe problem given the availability of computational power today.

C. Experimental Analysis

To analyze the performance of the proposed algorithm, at least two aspects are counted: its dependence on the waveform and robustness to noise. According to the CS theory, the performance of the recovery of a sparse signal from low-dimensional measurements depends on the coherence of dictionary. In the HRRP synthesis with a sparse SFW, the dictionary structure is closely related to the waveform. It is not difficult to see that the sparser SFW is, the less frequency observations are, which

TABLE I
RADAR PARAMETERS

f_0	PRF	T_i	Δf	B
10GHz	3kHz	20us	20MHz	320MHz

result in strong uncertainty in solving the optimization problem (22). Another factor, influencing the performance of the HRRP reconstruction with a sparse SFW is the underlying sparsity of the signal itself. In fact, the backscattering field of a man-made target usually has very few strong scattering centers presenting strong sparsity. However, when the energy of noise increases, the sparsity of the received signal degrades dramatically. To show the performance of the proposed algorithm, simulation is performed in the following. With reference to typical ISAR scenarios, the parameters to generate experimental data are based on a typical SF radar system operating with LFM-SFWs, which are listed in Table I. A target, composed of six dominant scattering centers, is simulated. Based on the system parameters, we need 16 subpulses for a full-band SFW with a CPI of 5.33 ms, approximately achieving range resolution about 0.47 m. In the simulation, we assume that each subpulse is sampled into a vector with $h = 64$ points, thus providing the HRRP with $L = 1024$ bins. In our experiment, we use three types of sparse SWFs (SSFWs), namely, SSFW1, SSFW2, and SSFW3. Each one consists of parts of the subpulses of the full-band SFW, taking one-fourth of the subpulses out from the full-band SFW evenly and giving the rest to SSFW1. Therefore, SSFW1 consists of 12 subpulses. Moreover, the amount of measurements of SSFW1 is $\overline{L}_1 = 768$. Every second subpulse pours to SSFW2, giving $\overline{L}_2 = 512$ measurements, and every fourth subpulse goes to form SSFW3, giving $\overline{L}_3 = 256$ frequency points. For clarity, the geometries of the sparse SF waveforms are given in Fig. 5. The complex white noise of Gaussian distribution is added into the simulated echoed signals to generate experimental signal with different SNRs (20, 10, and 5 dB). The radial velocity and acceleration are set as -100 m/s and -5 m/s^2, respectively. We assume that the range migration error caused by motion is corrected. In the following experiment, we figure out both motion-induced phase error and random phase error. We also analyze the effect of the selection of λ on the sparsity-driven HRRP synthesis. To evaluate the performance of the estimation of parameter λ, we give results generated by both the calculated λ and a experiential constant parameter. The following experiments are run on a personal computer with Core 2.53-GHz CPU and MATLAB.7.0.1. Furthermore, the sparsity-driven HRRP synthesizer is solved by using CG implemented by FFT and Hadamard multiplication.

In the first step, we only consider motion-induced phase error. Fig. 6 shows the phase error for a sequence of 16 subpulses in a curve form. This phase error produces distortion and spread of the HRRP. At first, we take $\lambda = 5$, δ is set as one in a thousand of the noise variance, and the iteration is terminated when $|\hat{\boldsymbol{\theta}}(g+1) - \hat{\boldsymbol{\theta}}(g)|_2 / |\hat{\boldsymbol{\theta}}(g)|_2 \leq 0.001$ for all SNR and waveform cases, and the results are shown in Fig. 7. This λ is selected manually after trying many values, and it should be relatively optimal under these simulation conditions.

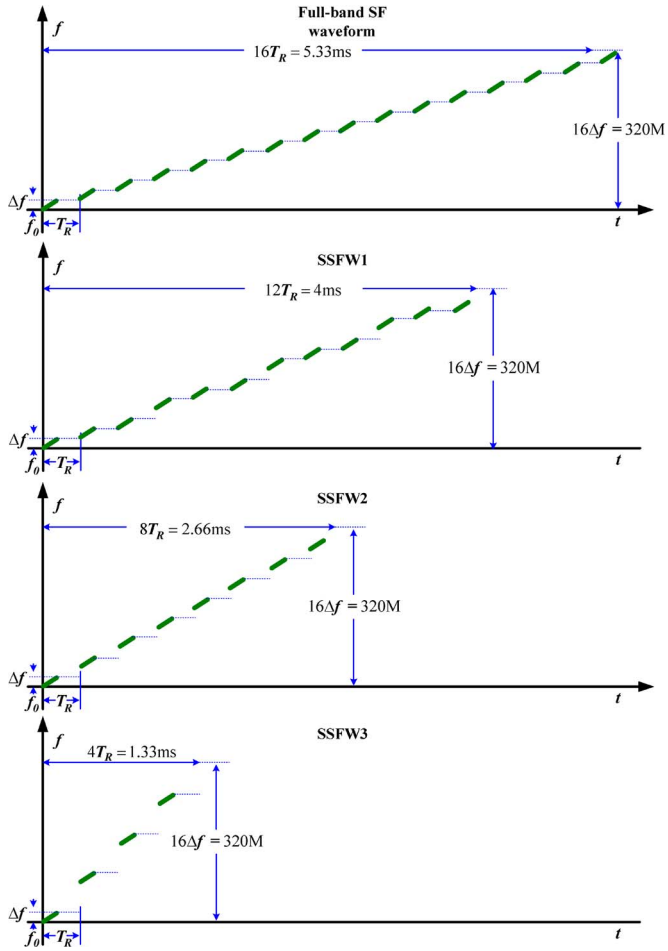

Fig. 5. Time–frequency profiles of the SSFWs.

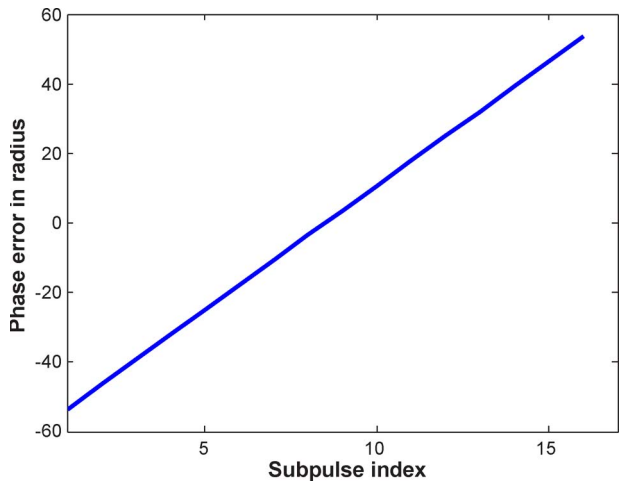

Fig. 6. Phase error caused by target motion.

In Fig. 7, the first row represents the experimental results of SSFW1 with different SNRs. The second and third rows in Fig. 7 show the results of SSFW2 and SSFW3, respectively. The expensed times for all experiment cases with $\lambda = 5$ are given in Table II. It is noted that, for all cases, the consuming time to generate an HRRP with the sparsity-driven approach is around 1–2 s. Moreover, comparing all these results, we find that all

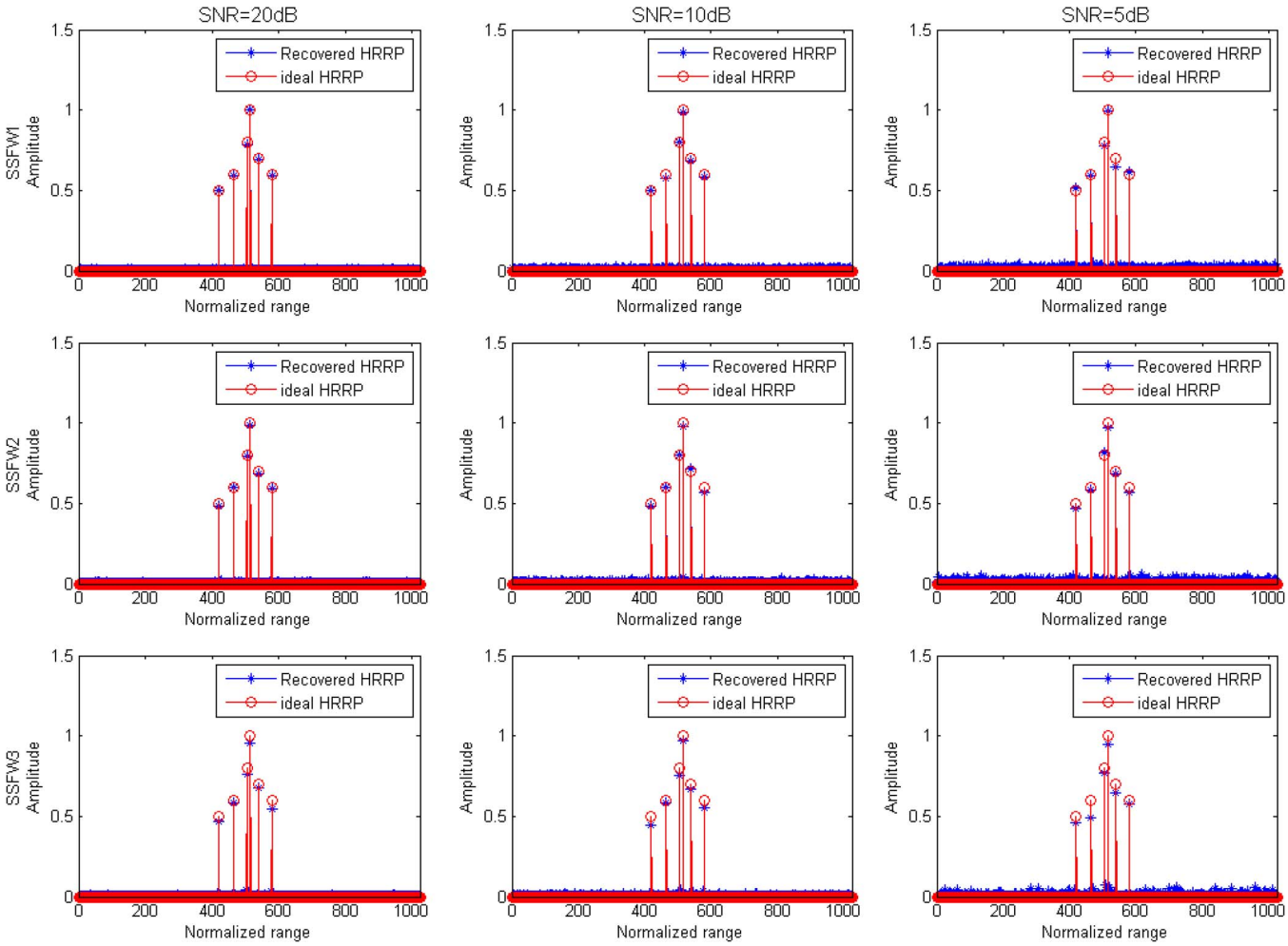

Fig. 7. Experimental results of sparse SFWs under different SNRs with $\lambda = 5$ (motion-induced phase error).

TABLE II
CONSUMING TIME (IN SECONDS) WITH $\lambda = 5$

	SNR=20dB	SNR=10dB	SNR=5dB
SSFW 1	1.321	1.312	1.527
SSFW 2	1.289	1.336	1.567
SSFW 3	1.519	1.838	2.358

TABLE III
PARAMETER λ

	SNR=20dB	SNR=10dB	SNR=5dB
SSFW 1	8.064	68.688	206.064
SSFW 2	7.911	64.328	189.118
SSFW 3	6.878	72.568	224.960

sparse SFWs provide good performance even in the case of low SNR, under the setting parameters. As expected, SSFW3 yields some distortion in the HRRP when SNR decreases to 5 dB while other waveforms overcome the strong noise effect at the same time. In the presence of strong noise, the HRRP synthesis tends to need more time to reach convergence than it does in the case of high SNR. The computational load also slightly relies on the amount of frequency measurements. Obtaining an HRRP with a very sparse SFW may involve a highly computational complexity.

Then, we still consider the motion-induced phase error in Fig. 6 and use an adaptive λ obtained by statistical parameter estimation. According to the statistical estimation of both noise and HRRP, the values of λ for all waveforms and SNR cases are listed in Table III. The terminating condition is still $|\hat{\boldsymbol{\theta}}(g+1) - \hat{\boldsymbol{\theta}}(g)|_2/|\hat{\boldsymbol{\theta}}(g)|_2 \leq 0.001$. Clearly, parameters are at an extent of 6–224 corresponding to the noise increase, all larger than 5. As aforementioned, larger λ usually leads to sparser HRRP and denoising performance. The results by using adaptive λ are shown in Fig. 8. The arrangement of them is identical to that of Fig. 7. The consuming times for all cases are given in Table IV. It is noted that, with an adaptive λ, generating an HRRP with the sparsity-driven approach is usually faster than with $\lambda = 5$. This indicates that by setting a larger λ, the efficiency of CG is usually increased. Therefore, we suggest a relatively large λ in the application of the approach as long as the precision meets the requirement. From the comparison of Figs. 7 and 8, we also conclude that the adaptive λ usually achieves better denoising

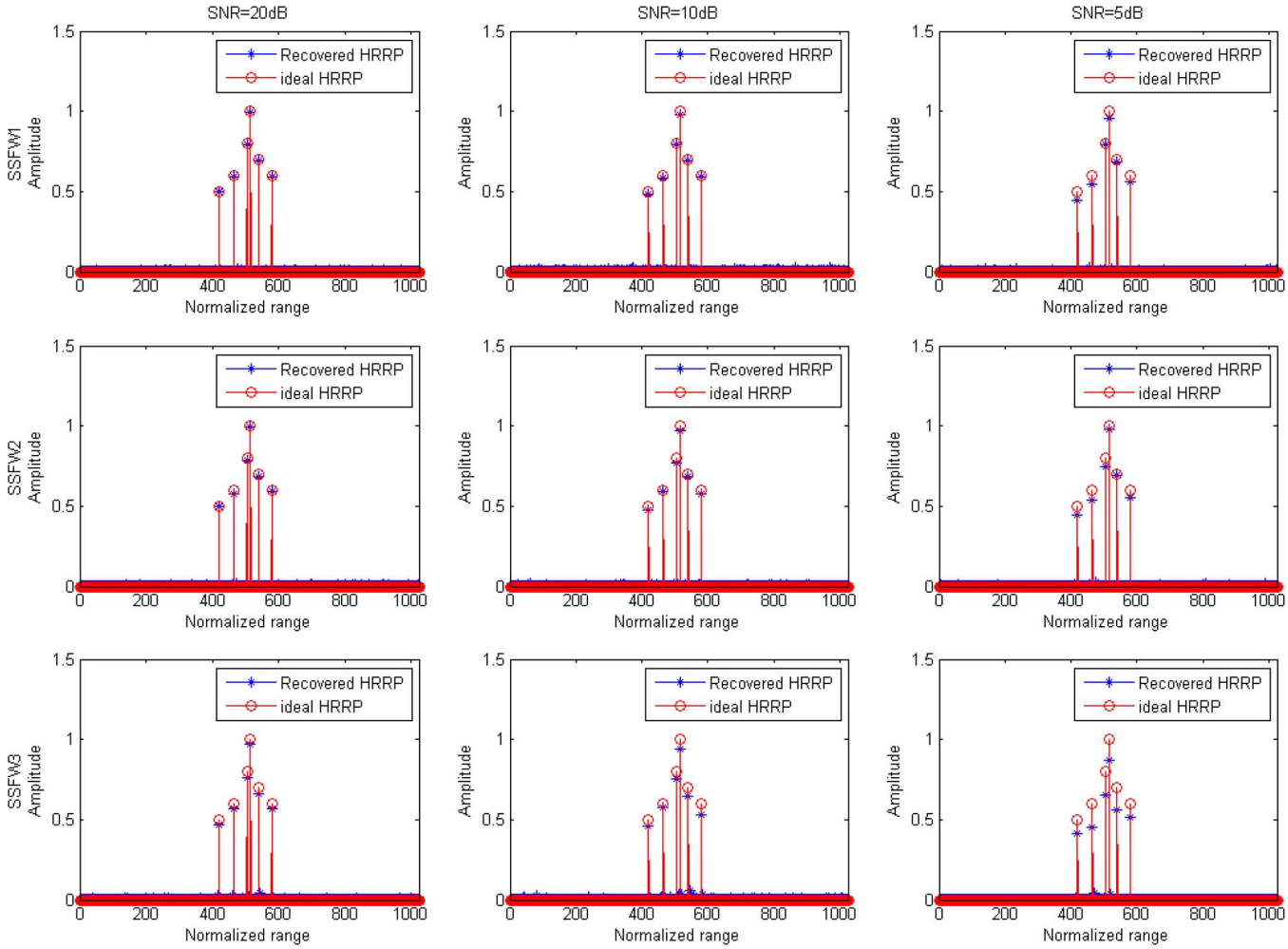

Fig. 8. Experimental results of sparse SFWs under different SNRs with adaptive λ (motion-induced phase error).

TABLE IV
CONSUMING TIME (IN SECONDS) WITH λ IN TABLE III

	SNR=20dB	SNR=10dB	SNR=5dB
SSFW 1	0.545	0.481	0.506
SSFW 2	0.608	0.528	0.689
SSFW 3	1.387	1.583	1.813

performance at a price of signal energy loss at some degree. For high contrast image, we think it is acceptable.

In the second step, we consider the motion-induced phase error along with errors from other sources. Thus, we assume that the phase error is random. Fig. 9 shows the random phase error for a sequence of 16 sweeps. Random phase error produces both profile distortion and false scatters, which make the HRRP useless. By exploiting the sparsity of the HRRP, we reduce the phase error to get the well-focused HRRP. At first, we still take $\lambda = 5$, δ is equal to one in a thousand of the noise variance, and the iteration is terminated when $|\hat{\boldsymbol{\theta}}(g+1) - \hat{\boldsymbol{\theta}}(g)|_2 / |\hat{\boldsymbol{\theta}}(g)|_2 \leq 0.001$. In Fig. 10, the experimental results of all SNR and waveform conditions are shown. From these results, all sparse

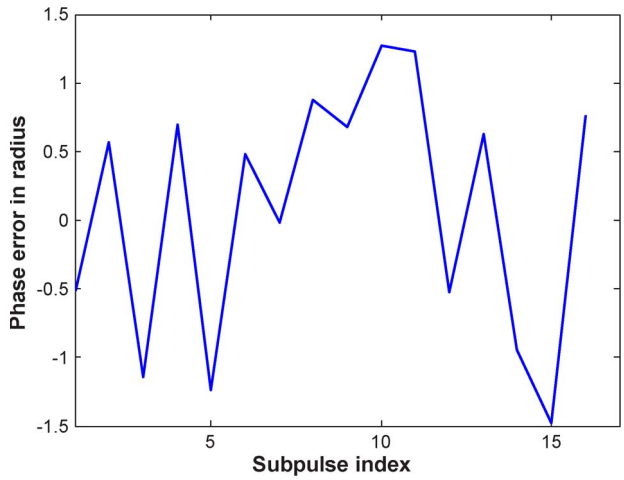

Fig. 9. Random phase error.

SFWs provide good performance, even in the case of low SNRs. The consuming time using the constant parameter is listed in Table V. The computational load, dependent on waveform and SNR, is identical to the results listed in Table II. Moreover, we also note that, in the case of random phase error, the sparsity-driven approach usually takes more time to go over it than in

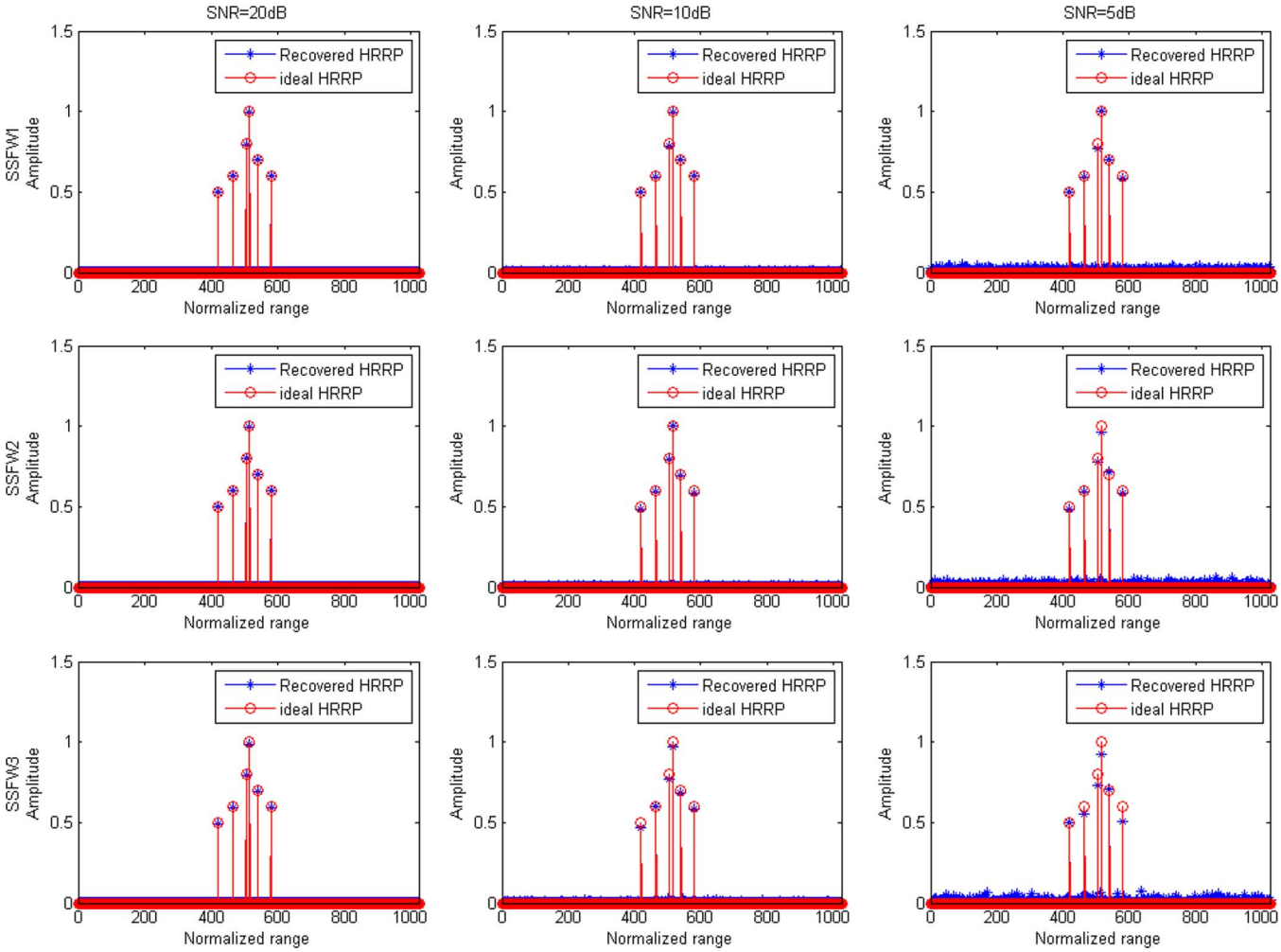

Fig. 10. Experimental results of sparse SFWs under different SNRs with $\lambda = 5$ (considering random phase error).

TABLE V
CONSUMING TIME (IN SECONDS) WITH $\lambda = 5$

	SNR=20dB	SNR=10dB	SNR=5dB
SSFW 1	2.697	3.435	4.977
SSFW 2	3.922	4.433	5.742
SSFW 3	4.917	6.217	8.840

the motion phase-error case. It is not difficult to understand that, in the random-phase case, the initialized solution is much farther than that in the linear phase-error case; therefore, the approach needs more iterations to get convergence. This means that the computational load increases as complex error (including both phase error and additive noise) is present. It is indicated that if precise phase-error correction is performed before using the sparsity-driven approach, its efficiency can be improved dramatically. This motivates our work of motion compensation in ISAR imaging in the next section. Also, this experiment confirms that the proposed method is applicable in wide scenarios and imposes no constraint on the formal phase error.

We still consider the random phase error and use adaptive λ. In this experiment, the adaptive parameters are identical to those listed in Table III. Furthermore, the terminating condition is still $|\hat{\boldsymbol{\theta}}(g+1) - \hat{\boldsymbol{\theta}}(g)|_2 / |\hat{\boldsymbol{\theta}}(g)|_2 \leq 0.001$. The results are shown in Fig. 11, and the consuming times are listed in Table VI. From the comparison of Figs. 10 and 11, we draw a similar conclusion on using the adaptive λ as in the comparison of Figs. 7 and 8.

IV. ISAR IMAGING WITH SPARSE SFWS

A. ISAR Imaging by Enhancing SNR and Sparsity

Conventional ISAR image processing with SF has three steps. First, the HRRP synthesis is performed, in which the target's motion should be estimated to avoid blurring and distortion of the HRRP. Then, the motion compensation including range alignment and phase adjustment is followed up to remove shift and phase errors among HRRPs. Finally, a 2-D high-resolution image is generated by compression in the cross-range, which is usually implemented by FFT. In our case, ISAR imaging with a sparse SFW, the key problem is to reconstruct the HRRP from sparse frequency measurements with phase errors. Given limited frequency samples containing noise,

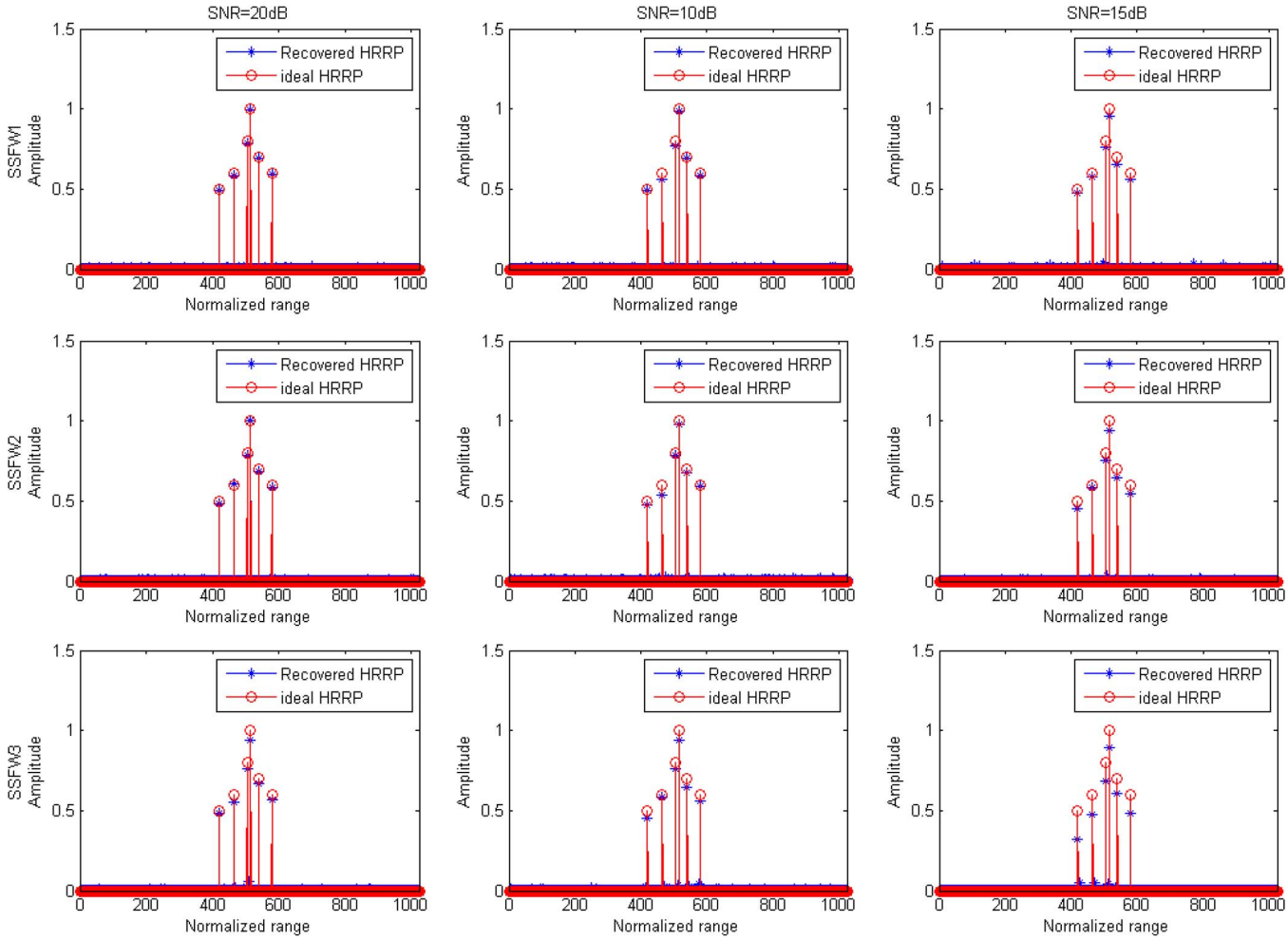

Fig. 11. Experimental results of sparse SFWs under different SNRs (considering random phase error).

TABLE VI
CONSUMING TIME (IN SECONDS) OF ADAPTIVE λ

	SNR=20dB	SNR=10dB	SNR=5dB
SSFW 1	0.702	0.774	0.900
SSFW 2	0.846	0.827	1.106
SSFW 3	2.495	2.803	2.745

generating the HRRP in a higher dimension is difficult. Through the exploitation of sparsity, the HRRP can be recovered from noisy sparse frequency (also see the last paragraph). Actually, an underlying condition for a successful HRRP synthesis is that the HRRP is composed of very limited dominant scattering centers. Even so, a truly subtle problem is how to estimate a considerable number of strong scattering centers from a limited set of SF subpulses to form the HRRP by the l_1-constrained optimization. The CS theory tells us that exact recovery from limited measurements can be carried out only for sparse signals. Nevertheless, the uncertainty involved in solving the optimization problem dramatically increases when strong noise is present due to degradation of signal sparsity. It is not difficult for one to understand that the lower SNR of the measurements is, the more difficult it is to obtain the precise recovery of the HRRP with sparse SFWs. Due to the aforementioned facts, the SNR enhancement should be taken into account before performing the HRRP synthesis for the ISAR imaging with sparse SFWs.

Modern radar systems employ coherent integrals for effective detection and identification of weak signals submerged in strong noises. The coherent integral is usually implemented by the FFT banks. In this way, signal energy is fully accumulated to improve the SNR, while the noise energy is still spreading over the whole space. As we know, the improvement of the SNR gain is proportional to the amount of data in coherent processing: If the number of data doubles, the SNR approximately increases by 3 dB. Based on this, we are now proposing a new framework to improve the performance of ISAR imaging with a sparse SFW. In the framework, we modify the coherent integral to each subpulse in the cross-range before the HRRP synthesis, which provides a high SNR gain for measurements. Another benefit from the coherent integral is the enhancement of the HRRPs' sparsity to recover the ISAR image. The coherent integral resolves dominant scatters in sets of Doppler cells. Each Doppler cell contains only a few scatters. Therefore, both accuracy and efficiency of the HRRP synthesis for each Doppler cell are dramatically improved. The framework of the

ISAR imaging with sparse SFWs runs in the following three steps.

1) Subpulses in each subband is extracted from bursts and arranged into a consistent set. Then, for each group, range alignment and phase compensation are applied to eliminate the bulk motion.
2) The FFT in the cross-range is employed for each group to generate subband ISAR images.
3) Noise variance estimation is performed by using the coarse 2-D images. Fourier transform in range is taken to transform each subband ISAR image into the range frequency and Doppler domain. Finally, the HRRP synthesis is performed in (18) to overcome the residue phase error and achieve the high resolution of a 2-D ISAR imagery. In the HRRP synthesis, parameter λ calculated for each Doppler bin independently.

Step 1) is essential when one applies sparse SFWs to generate the high-resolution ISAR image, as motion compensation plays a significant role in both the HRRP synthesis and the ISAR imaging. In step 1), on the basis of the assumption that the radar system is coherent, time delays and high-order phases caused by target bulk motion are compensated to each subband group. For the HRRPs, conventional range alignment methods [26]–[28] are employed to estimate time delays of range profiles and thus obtain motion parameters (velocity and acceleration) of the moving target by low-order polynomial fitting. However, the accuracy of motion estimation degrades by using these techniques in the subband range profiles due to the resolution limitation of subband range profiles. Hence, we need to combine some motion approaches successively in order to get a precise estimation of a bulk motion from subband data sets.

First, we estimate coarse velocity by range alignment techniques. Then, we can obtain the shift of range profiles that matches a polynomial function whose first order term gives the coarse velocity. Based on the coarse velocity, the range cell migration of range profiles would be reduced to a nominal degree. Second, a cross-correlation function among adjacent range profiles is used to evaluate acceleration. Adjacent cross-correlation is proven effective to estimate translational motion of the moving target robustly, particularly for the acceleration. The acceleration estimation can be transferred into a problem to evaluate high-order phase terms by autofocus techniques [26], [39]–[42]. Then, by fitting the phase function into a two-order polynomial function, the second-order coefficient is corresponding to the acceleration of the target. Generally, the estimation based on the adjacent cross-correlation is capable of sustaining strong noise due to the application of coherent accumulation, and its efficiency is high by applying FFT to calculate the adjacent cross-function [43]. Finally, the residual velocity is obtained from the Doppler centroid of the target in the RD plane. It should be pointed out that the major velocity effect is eliminated by the compensation with the coarse velocity, but the residual effect may still not be nominal. In low PRF cases where the residual velocity is great, the Doppler centroid may be ambiguous. To resolve the ambiguity of the Doppler centroid, the multifrequency characteristics of sparse SFWs should be taken into account to resolve the Doppler centroid ambiguity [44]–[46]. To resolve the ambiguity of Doppler centroids, the Chinese remainder theorem (CRT) [45] can be applied. To improve the performance of CRT in the presence of strong noise, improvement has been done in [46]. Herein, we propose another robust method to solve this ambiguity. Let $D_m = 2f_{sm}\Delta v/c$ be the unambiguous Doppler centroid caused by residue velocity (Δv) of the mth subband group. Due to the low PRF, we have the ambiguous estimate as $\Delta\hat{D}_m = \text{mod}(D_m, PRF) + e_m$ and e_m denotes the estimate error. After coarse velocity compensation, the residue velocity is relatively small. The ambiguity number for each carrier frequency is equal to U (U is an integer). Clearly, if we know the ambiguity number, Δv can be estimated from $\Delta\hat{D}_m$, which is given by

$$\Delta\hat{v}(N) = \frac{1}{M}\sum_{m=1}^{M}\frac{(U\cdot PRF + \Delta\hat{D}_m)\cdot c}{2f_{sm}}. \tag{34}$$

Due to the random property of the estimate error, the averaging processing in (34) is capable of providing a precise estimate of residue velocity. In this sense, we can shift the problem of estimating residue velocity to a problem of estimating the ambiguity number. Using (34), a penalty function of ambiguity number is developed as

$$P(u) = \sum_{m=1}^{M}\left(\frac{(u\cdot PRF + \Delta\hat{D}_m)\cdot c}{2f_{sm}} - \Delta\hat{v}(u)\right)^2. \tag{35}$$

Clearly, the penalty function reaches its minimum at U. This ambiguity-resolving approach is simple but robust. Furthermore, the real residue velocity is retrieved accurately by (34).

By using these robust motion-estimation approaches, we can perform motion compensation using the parameters already estimated. To keep the coherence among subbands, all the motion parameters involved are identical to all subbands. For clarity, we provide a useful flowchart of the bulk-motion compensation in this step in Fig. 12.

In step 2), standard Fourier-based pulse-compression methods are used to generate the coarse 2-D images of the target for each subband group data. Since each image is associated with a narrow bandwidth, the range resolution is relatively low. However, the high resolution in cross-range is achieved and dominant scatters are resolved in many Doppler cells. Some linear spectral estimation techniques [12] can be applied to achieve superresolution in cross-range and preserve the mutual coherence among subbands. The cross-range compression in this step provides high SNR gain, which is useful to the next step of HRRP synthesis for each Doppler cell in both precision and efficiency. Another benefit from the cross-range compression is the enhancement of the HRRPs' sparsity for each Doppler bin as the compression resolves scatters into a set of Doppler cells, each of which contains only a few scatters rather than all scatters of the target. Clearly, due to the sparsity enhancement, the performance of the sparsity-driven HRRP synthesizer is improved with relaxation on the amount of measurements to generate a high-resolution ISAR image.

In step 3), the HRRP synthesis is performed to coherently combine coarse images of the sparse subbands to yield a

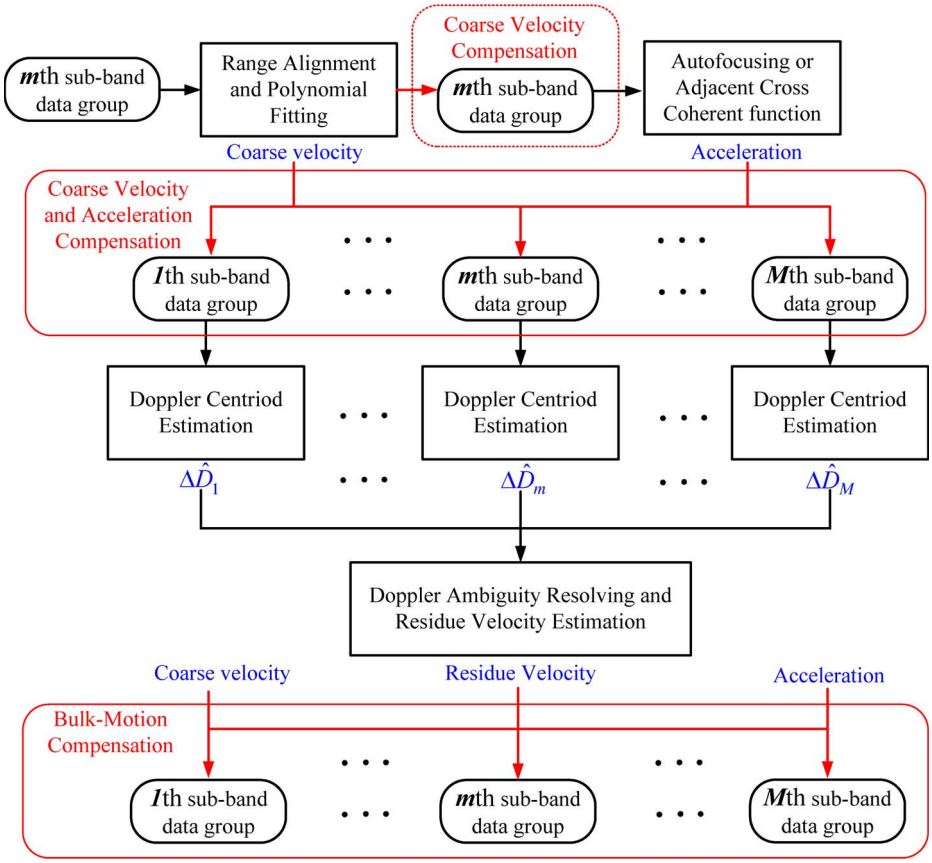

Fig. 12. Flowchart of the motion compensation for SFM ISAR imagery.

2-D image with 2-D high resolution. After azimuth compression in step 2), scattering centers of the target are distributed over sets of Doppler cells. The sparsity together with SNR is dramatically enhanced for each Doppler cell, which allows us to coherently fuse sparse band data into the HRRPs even when strong noise is present. The HRRP synthesis in this step is performed to each of the Doppler bins. At first, the low-resolution range profiles corresponding to a Doppler cell in coarse images are extracted. The statistics of noise and range profiles are estimated from the subband range profiles, and then, the parameter λ can be calculated for each Doppler bin. Then, the signals corresponding to the range bin are transformed into range frequency domain, and the sparsity-driven HRRP synthesizer is applied. Because of the motion compensation in step 1), residual phase errors are small in quantity but may still bring blurs and false scatters in the HRRP synthesis. Therefore, the HRRP synthesis may take several iterations to overcome the residual errors adaptively. The same process is performed to every Doppler bin, and the high-resolution ISAR imagery is generated. This process can be performed by parallelizing over Doppler bins. Thus, the algorithm can take advantage of multiple processors and special hardware and software for FFTs and Hadamard multiplication in the implementation of the approach, such as field-programmable gate array. Therefore, the real-time implementation of the sparsity-driven imaging approach is possible.

It should be noted in this step that, given a set of coarse 2-D ISAR images in hand, we can select noise samples directly from them based on the assumption of even noise distribution. Since the target support should take only a fraction of the image plane, the noise bins are very abundant in the coarse images. Clearly, the application of the energy-based threshold in (23) and the wide-band CFAR detection in (25) to 2-D data is straightforward. For clarity, a detailed procedure for this step is shown in Fig. 13.

B. Performance Analysis With Both Simulated and Measured Data

In this section, both simulated and real experimental data are used for taking a performance analysis of the ISAR image with sparse SFWs. The performance analysis is carried out by considering two factors: the tolerance of noise and the reliance on waveform. First, we use the simulated data. The data are generated with the radar parameters listed in Table I and a scattering model of the Yak-42 plane. A total of 128 bursts are produced, and each burst consists of 16 sub-pulses for a full-band SFW. The scattering point model of target is shown in Fig. 14. To analyze the imaging performance of dependence on waveform, the three types of sparse SFWs in the experiments in Section III are used to generate measurements of sparse frequency bands. The complex noise with Gaussian distribution is added into simulated echoes to obtain different SNRs (20, 10, and 5 dB). The radial velocity and acceleration of plane are set as -100 m/s and -5 m/s^2, respectively. The low-range profiles are shown in Fig. 15, where the range migration is obvious due to the radial motion.

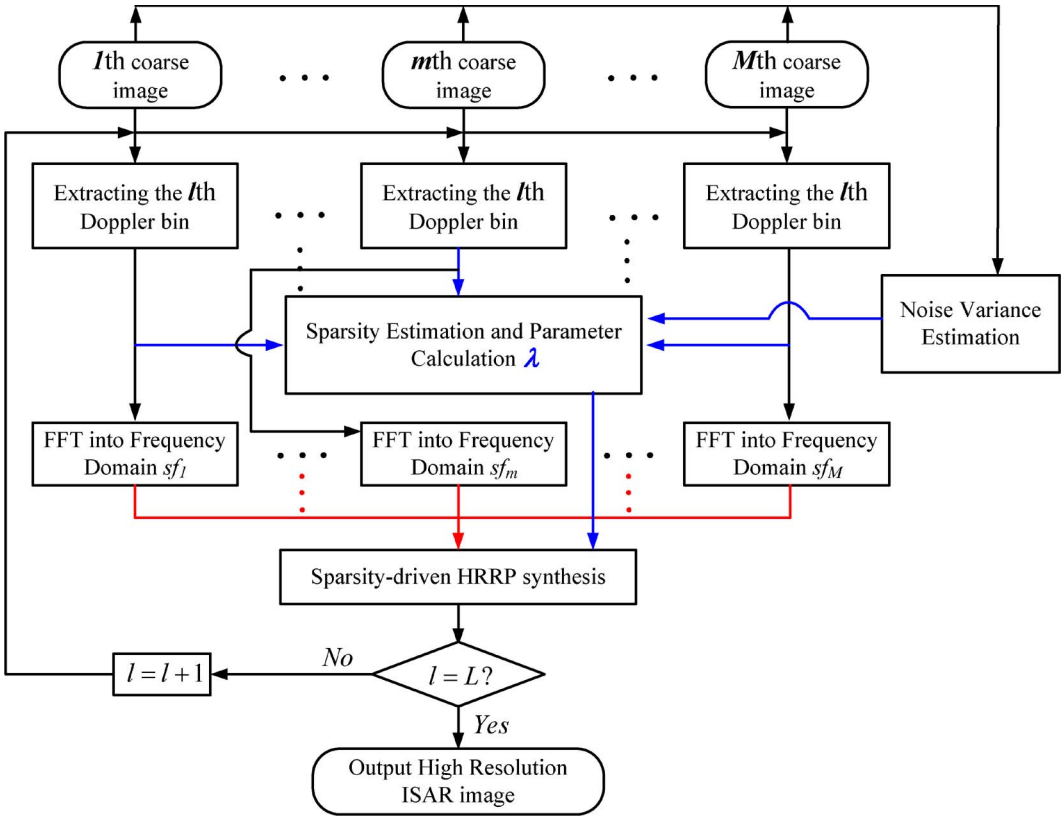

Fig. 13. HRRP synthesis and high-resolution image generation.

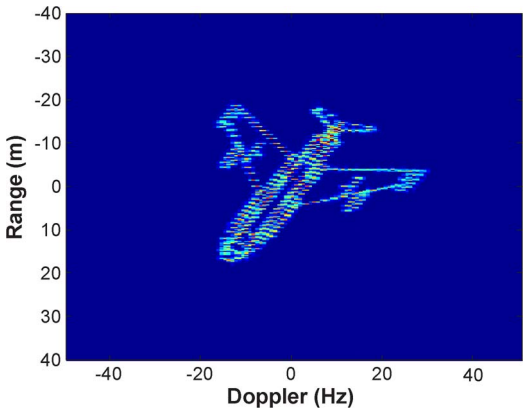

Fig. 14. Scattering model of Yak-42 plane.

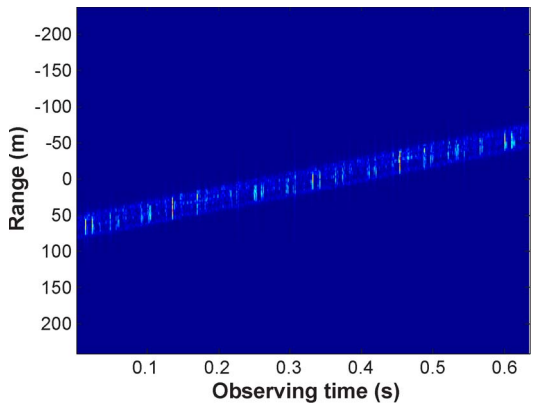

Fig. 15. Simulated range profiles.

With different SNRs, three sparse SFWs shown in Fig. 5 are tested. The experiment flow follows the three steps of ISAR imaging. The radial motion estimations are given in Table VII, which are accurate at the predetermined SNR cases. In the case of SNR $= 5$ dB, after coarse velocity compensation, the residual velocity brings Doppler ambiguity. Ambiguity should be resolved from the Doppler centroids of several subband images. In our experiment, the proposed ambiguity-resolving approach is employed to sustain an estimation error of Doppler centroids present in the case of SNR $= 5$ dB. The reconstructed high-resolution ISAR images are shown in Fig. 16. In the HRRP synthesis, λ is calculated adaptively according to the statistical parameters estimation, and the iteration of HRRP synthesis is terminated when $|\hat{\boldsymbol{\theta}}(g+1) - \hat{\boldsymbol{\theta}}(g)|_2 / |\hat{\boldsymbol{\theta}}(g)|_2 \leq 0.001$. In Fig. 16, the first row represents experimental results of SSFW1 with different SNRs. The second and third rows in Fig. 16 show the results of SSFW2 and SSFW3 corresponding to different

TABLE VII
RADIAL MOTION ESTIMATION

	SNR=20dB	SNR=10dB	SNR=5dB
Velocity estimation (m/s)	-99.9845	-99.9790	-99.9513
Acceleration estimation (m/s^2)	-4.9622	-4.9623	-4.9633

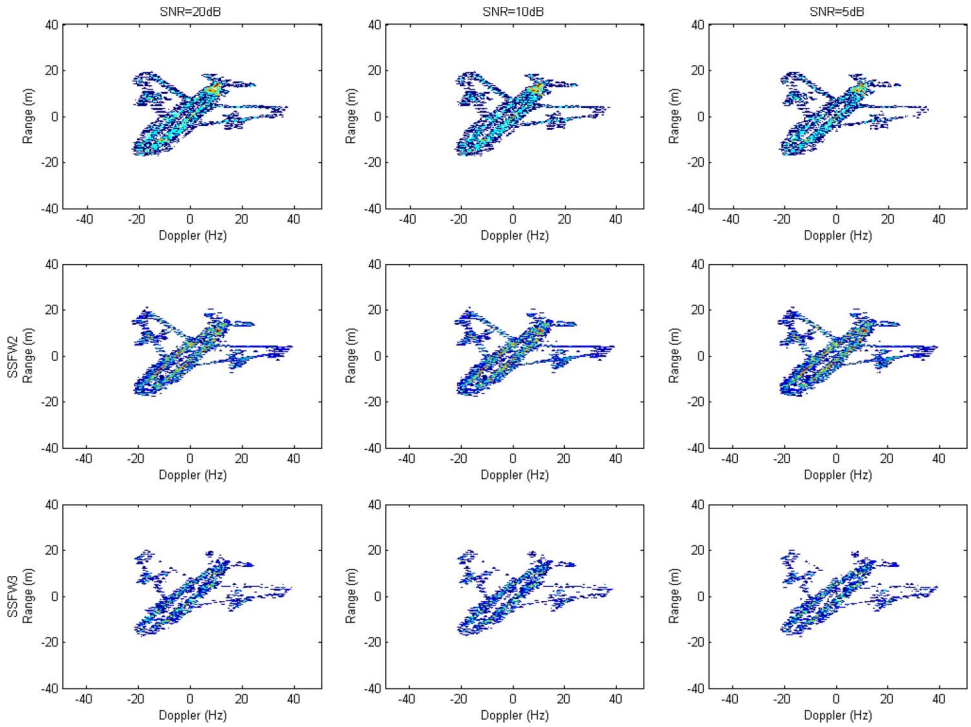

Fig. 16. Results with the proposal sparse SFWs under different SNRs.

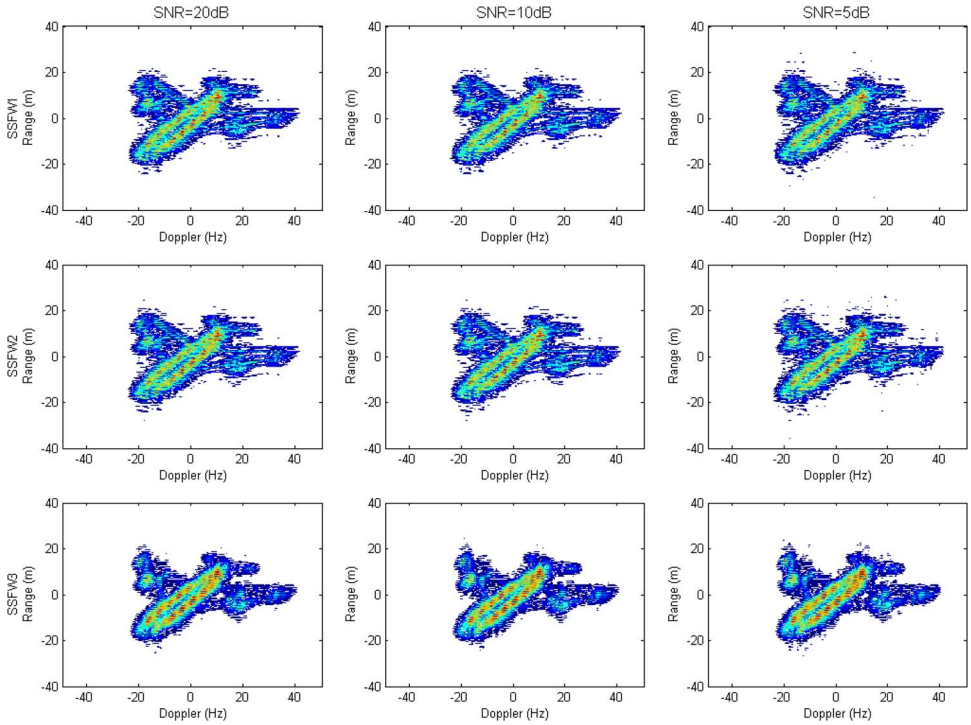

Fig. 17. Results with zero-padding FFT of sparse SFWs under different SNRs.

SNRs, respectively. Imaging results are optimal even in the case of SSFW3 and SNR $= 5$. Owing to the coherent integrant of cross-range compression and precise motion estimation, both quality and efficiency of the HRRP synthesis with sparse SFWs are enhanced. These results match the proposed ISAR imaging framework with sparse SFWs. By comparing results with different sparse SFWs, we conclude that the denser the waveform is, the more scattering centers can be extracted. Sparse SFM waveform is a special kind of thinned waveforms [11], but its frequency properties are different from that of random thinned waveforms. Its subbands have identical bandwidths, and the vacant frequency band between adjacent subbands is usually wide. Sparse SF waveforms provide flexibility and convenience in radar system design. By applying sparse SF waveforms, we can furnish some active narrow bandwidth radars with imaging capability by nominal adjustment in signal generation.

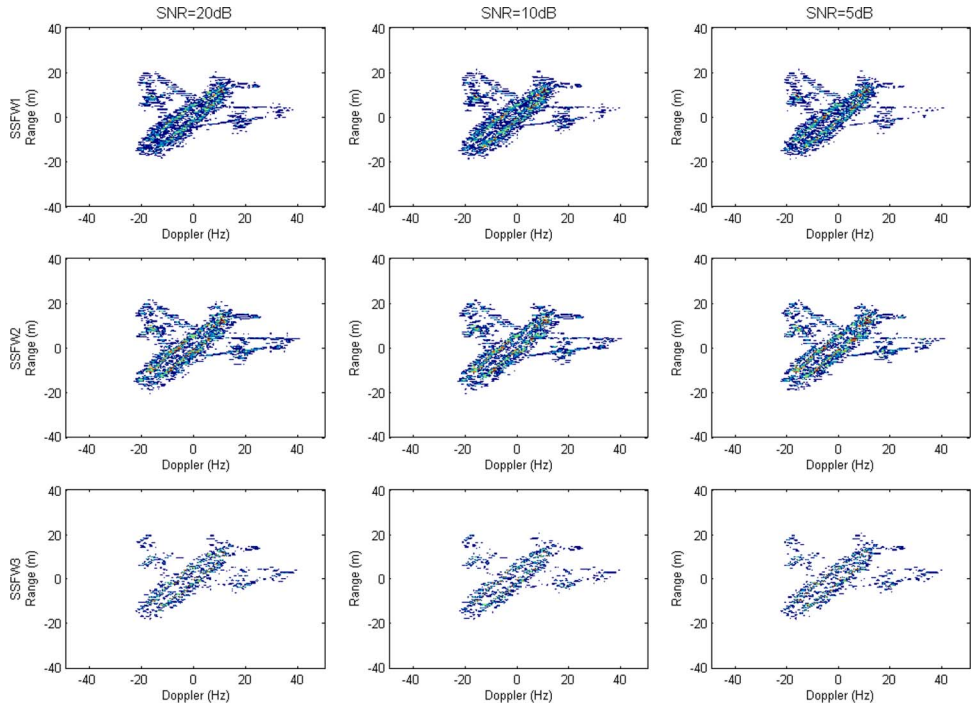

Fig. 18. Results with S-CLEAN sparse SFWs under different SNRs.

Fig. 19. Photo of the observed ship.

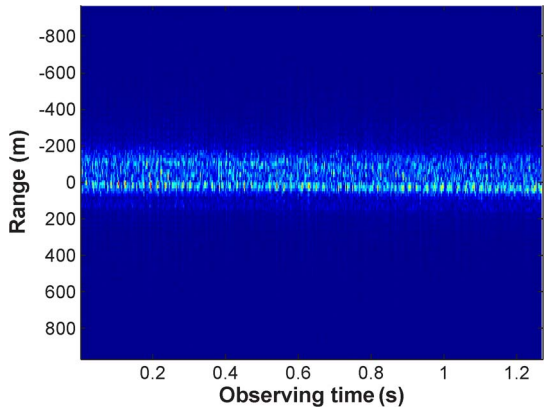

Fig. 20. Range profiles of the ship.

TABLE VIII
EXPERIMENTAL RADAR PARAMETERS

f_0	PRF	T_i	Δf	B
5.57GHz	3.125kHz	10us	20MHz	640MHz

TABLE IX
ESTIMATION OF SHIP RADIAL MOTION

	SNR=20dB	SNR=10dB	SNR=5dB
Velocity estimation (m/s)	2.1982	2.1978	2.2036
Acceleration estimation (m/s^2)	0.1020	0.1030	0.1076

However, the system response of sparse SF waveforms is with not only high sidelobes but also high grating lobes. Therefore, the images generated by IFFT are blurred and along with a lot of false points and their resolutions are low, as shown in Fig. 17. As a result, images obtained by IFFT might be useless for further applications, such as target recognition. In IFFT imaging, the vacant frequency bands are zero padded, and then, IFFT is applied to the signal in frequency domain. Aside from the sparsity-driven approach, some novel methods are also capable of overcoming high sidelobes of system response. The S-CLEAN algorithm [47] was proposed to deal with thinned frequency waveforms in [11]. It is an iterative deconvolution algorithm capable of resolving close targets even in the case that the system response is heavily affected by high sidelobes. S-CLEAN algorithm performs well in imaging with random thinned waveforms [11]. In addition, it should be emphasized that S-CLEAN algorithm requires precise motion compensation. For comparison, we also use the S-CLEAN algorithm to the data sets of the sparse SF waveforms. In terms of consistency, S-CLEAN is applied in HRRP synthesis, replacing our

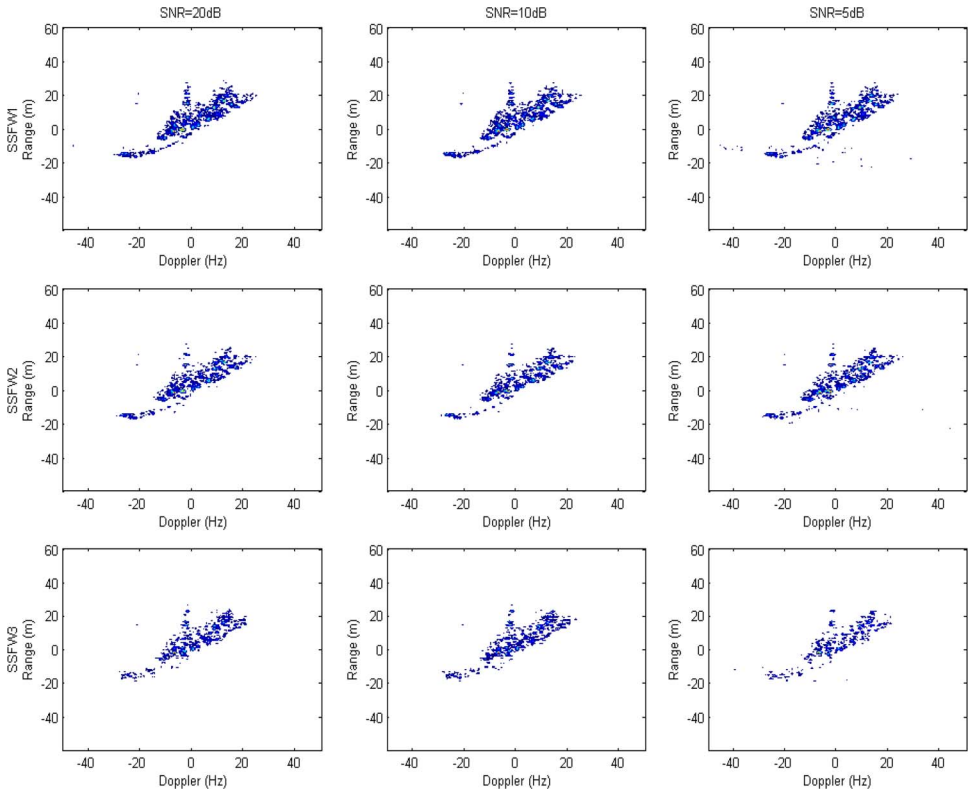

Fig. 21. Results with the proposal of sparse SFWs under different SNRs with real data.

method after the same motion compensation. The results from S-CLEAN are shown in Fig. 18, whose arrangement is identical to that in Fig. 16. Clearly, similar to our sparsity-driven approach, S-CLEAN overcomes sidelobes and grating lobes effectively. Comparing Fig. 18 with Fig. 16, one can find that edge of the target in S-CLEAN images is not as distinctive as in sparsity-driven images, along with some scatter losses. It is indicated that, in dealing with sparse SF waveform signal, our approach provides image with higher contrast and precision than those of S-CLEAN at the price of larger computational load.

Here, we provide experimental results with real measured ISAR data with a full-band SFW from a ship in the sea. The ship photograph is shown in Fig. 19. The parameters of the experimental SF radar are listed in Table VIII. In real situations, the radar is located at an elevation of about 100 m above sea level. The relative aspect angle between the radar light of slight and ship track is about 45°. During the observing time, the radar transmits 32 SFM subpulses as a burst, providing a range resolution of 0.234 m. In the experiments, 128 bursts are used, and the range profiles are shown in Fig. 20. We extract portions of subpulses to form echoes from sparse SFWs. The three sparse waveforms are assumed: extracting one-fourth of the subpulses out from the full-band SFW evenly and the rest gives SSFW1, every second subpulse pours to SSFW2, and every fourth subpulse goes to form SFW3. Their geometries are similar to those shown in Fig. 5, but their amounts of subpulses are 24, 16, and 8, respectively. The experimental data have high SNRs up to 20 dB approximately. To perform a quality analysis under different SNR conditions, we add complex Gaussian noise into the echoes to generate measurements with different SNRs (20, 10, and 5 dB). The motion of the ship is estimated and listed in Table IX. The imaging results with different sparse SFWs and SNRs are shown in Fig. 21. The λ for the HRRP synthesis is calculated from the adaptive statistical estimation, and the iteration is terminated when $|\hat{\boldsymbol{\theta}}(g+1)-\hat{\boldsymbol{\theta}}(g)|_2/|\hat{\boldsymbol{\theta}}(g)|_2 \leq 0.001$. In Fig. 21, the first row represents imaging results of SSFW1 with different SNRs. The second and third rows present imaging results of SSFW2 and SSFW3 corresponding to different SNRs, respectively. Our imaging framework with sparse SFWs provides good imaging quality, even in the case of significant frequency bands missing and in the presence of strong noise. In terms of comparison, we also provide image results with IFFT and the S-CLEAN algorithm in Figs. 22 and 23, respectively. Although we can still find that significant improvement is achieved by S-CLEAN over the IFFT imaging, some degradations are still present in S-CLEAN images by comparing them with those generated by the sparsity-driven method. The images generated by the sparsity-driven method are usually constructed in a denser and cleaner way than those from S-CLEAN at the expense of computation complexity. In sparsity-driven images, the edge of the ship is distinctive to represent the shape and geometry of the target. Then, we believe the sparsity-driven approach for high-resolution ISAR imaging with sparse SF waveforms is deemed useful in real applications, particularly when it is parallelized by taking the advantage of some multiple processors in real-time implementation.

V. Conclusion

SSFWs have more superiorities than conventional SFWs, such as shorter data acquisition interval, smaller data amount,

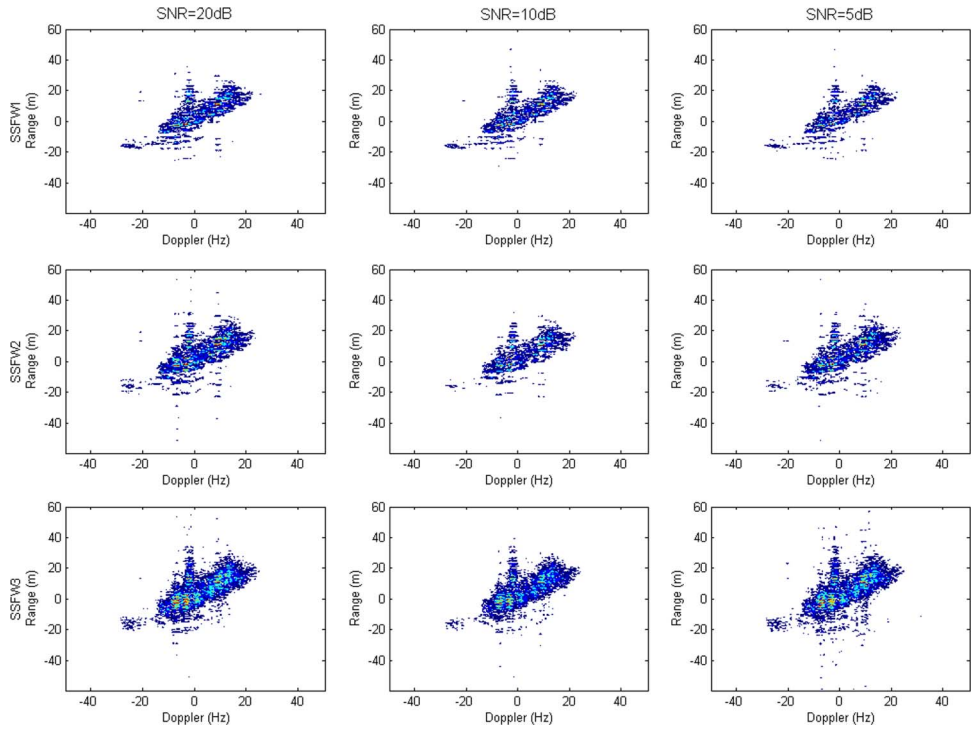

Fig. 22. Results with zero-padding FFT of sparse SFWs under different SNRs with real data.

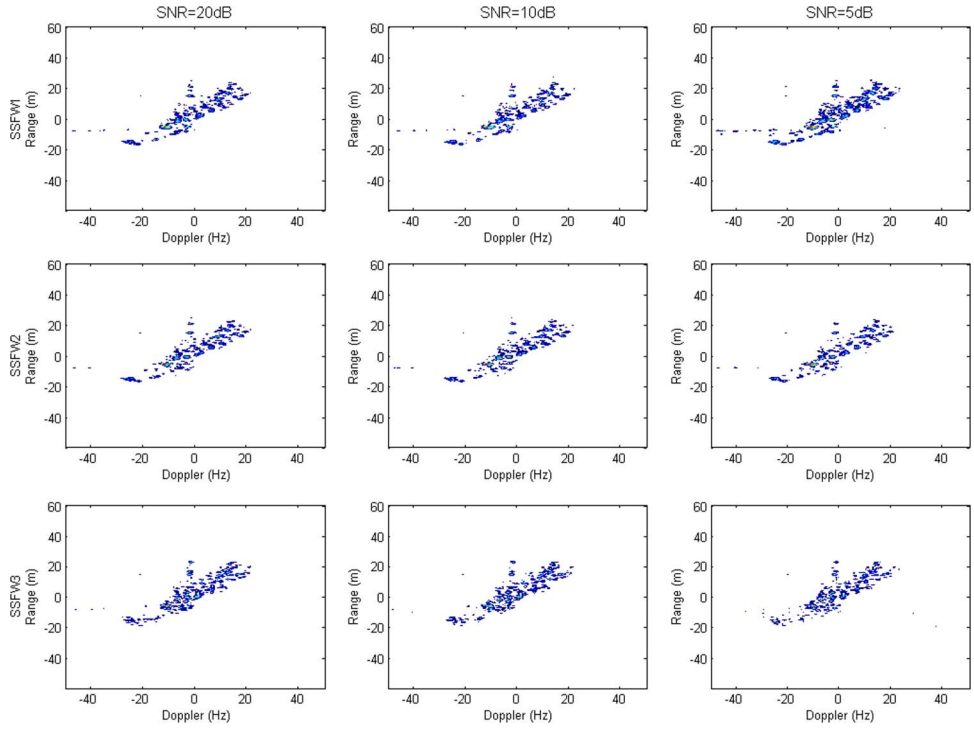

Fig. 23. Results with S-CLEAN of sparse SFWs under different SNRs with real data.

and better antijamming capability. However, the high-resolution ISAR imaging with sparse SFWs encounters difficulties caused by missing data. In this paper, we have proposed a novel framework for high-resolution ISAR imaging with SSFWs by exploiting the spatial sparsity of ISAR signal. In the framework, motion estimation has three steps and provides accurate estimation under low SNRs. The imaging flow is modified to enhance signal sparsity and SNR before the HRRP synthesis. One may achieve the high-quality resolution imagery by using our method robustly, even if the limited frequency measurements are affected by strong noise. We believe that its robustness makes it useful to suppress the noise and light requirement of

waveforms in real applications of radar imaging. Further works to improve the efficiency and real-time implementation of the sparsity method are underway.

ACKNOWLEDGMENT

The authors would like to thank the anonymous reviewers for their valuable comments to improve the paper quality.

REFERENCES

[1] D. R. Wehner, *High Resolution Radar*. Norwood, MA: Artech House, 1995.

[2] Q. Zhang and Y. Q. Jin, "Aspects of radar imaging using frequency-stepped chirp signals," *EURASIP J. Appl. Signal Process.*, vol. 2006, pp. 1–8, 2006, Article ID 85823.

[3] S. R. J. Axelsson, "Analysis of random step frequency radar and comparison with experiments," *IEEE Trans. Geosci. Remote Sens.*, vol. 45, no. 4, pp. 890–904, Apr. 2007.

[4] G. S. Gill, "Step frequency waveform design and processing for detection of moving targets in clutter," in *Proc. IEEE Int. Radar Conf.*, May 8–11, 1995, pp. 573–578.

[5] Y. Luo, Q. Zhang, C. Qiu, X. Liang, and K. Li, "Micro-Doppler effect analysis and feature extraction in ISAR imaging with stepped-frequency chirp signals," *IEEE Trans. Geosci. Remote Sens.*, vol. 48, no. 4, pp. 2087–2098, Apr. 2010.

[6] F. Berizzi, M. Martorella, A. Cacciamano, and A. Capria, "A contrast-based algorithm for synthetic range-profile motion compensation," *IEEE Trans. Geosci. Remote Sens.*, vol. 46, no. 10, pp. 3053–3062, Oct. 2008.

[7] H. Chen, Y. Liu, W. Jiang, and G. Guo, "A new approach for synthesizing the range profile of moving targets via stepped-frequency waveforms," *IEEE Geosci. Remote Sens. Lett.*, vol. 3, no. 3, pp. 406–409, Jul. 2006.

[8] H.-R. Jeong, H.-T. Kim, and K.-T. Kim, "Application of subarray averaging and entropy minimization algorithm to stepped-frequency ISAR autofocus," *IEEE Trans. Antennas Propag.*, vol. 56, no. 4, pp. 1144–1154, Apr. 2008.

[9] T. Lamont-Smith, R. D. Hill, S. D. Hayward, G. Yates, and A. Blake, "Filtering approaches for interference suppression in low-frequency SAR," *Proc. Inst. Elect. Eng.—Radar Sonar Navig.*, vol. 153, no. 4, pp. 338–344, Aug. 2006.

[10] T. Miller, L. Potter, and J. McCorkle, "RFI suppression for ultra wideband radar," *IEEE Trans. Aerosp. Electron. Syst.*, vol. 33, no. 4, pp. 1142–1156, Oct. 1997.

[11] A. Freedman, R. Bose, and B. D. Steinberg, "Thinned stepped frequency waveforms to furnish existing radars with imaging capability," *IEEE Aerosp. Electron. Syst. Mag.*, vol. 11, no. 11, pp. 39–43, Nov. 1996.

[12] S. L. Borison, S. B. Bowling, and K. M. Cuomo, "Super-resolution methods for wideband radar," *Lincoln Lab. J.*, vol. 5, no. 3, pp. 441–461, 1992.

[13] H. C. Stankwitz and M. R. Kosek, "Sparse aperture fill for SAR using super-SVA," in *Proc. IEEE Nat. Radar Conf.*, Ann Arbor, MI, May 13–16, 1996, pp. 70–75.

[14] X. Xu and R. M. Narayanan, "Enhanced resolution in SAR/ISAR imaging using iterative sidelobe apodization," *IEEE Trans. Image Process.*, vol. 14, no. 4, pp. 537–547, Apr. 2005.

[15] M. Çetin and W. C. Karl, "Feature-enhanced synthetic aperture radar image formation based on nonquadratic regularization," *IEEE Trans. Image Process.*, vol. 10, no. 4, pp. 623–631, Apr. 2001.

[16] E. Candès, J. Romberg, and T. Tao, "Robust uncertainty principles: Exact signal reconstruction from highly incomplete frequency information," *IEEE Trans. Inf. Theory*, vol. 52, no. 2, pp. 489–509, Feb. 2006.

[17] E. Candès, J. Romberg, and T. Tao, "Near-optimal signal recovery from random projections: Universal encoding strategies?," *IEEE Trans. Inf. Theory*, vol. 52, no. 2, pp. 489–509, Feb. 2006.

[18] D. Donoho, "Compressed sensing," *IEEE Trans. Inf. Theory*, vol. 52, no. 4, pp. 5406–5425, Apr. 2006.

[19] L. Zhang, M. Xing, C. Qiu, J. Li, and Z. Bao, "Achieving higher resolution ISAR imaging with limited pulses via compressed sampling," *IEEE Geosci. Remote Sens. Lett.*, vol. 6, no. 3, pp. 567–571, Jul. 2009.

[20] L. Zhang, M. Xing, C. Qiu, J. Li, J. Sheng, Y. Li, and Z. Bao., "Resolution enhancement for inversed synthetic aperture radar imaging under low SNR via improved compressive sensing," *IEEE Trans. Geosci. Remote Sens.*, vol. 48, no. 10, pp. 3824–3838, Oct. 2010.

[21] K. R. Varshney, M. Çetin, J. W. Fisher, and A. S. Willsky, "Sparse representation in structured dictionaries with application to synthetic aperture radar," *IEEE Trans. Signal Process.*, vol. 56, no. 8, pp. 3548–3561, Aug. 2008.

[22] A. C. Gurbuz, J. H. McClellan, and W. R. Scott, "A compressive sensing data acquisition and imaging method for stepped frequency GPRs," *IEEE Trans. Signal Process.*, vol. 57, no. 7, pp. 2640–2650, Jul. 2009.

[23] X. Zhu and R. Bamler, "Tomographic SAR inversion by L_1-norm regularization—The compressive sensing approach," *IEEE Trans. Geosci. Remote Sens.*, vol. 48, no. 10, pp. 3839–3846, Oct. 2010.

[24] A. Budillon, A. Evangelista, and G. Schirinzi, "Three-dimensional SAR focusing from multipass signals using compressive sampling," *IEEE Trans. Geosci. Remote Sens.*, vol. 49, no. 1, pp. 488–499, Jan. 2011.

[25] I. G. Cumming and F. H. Wong, *Digital Processing of Synthetic Aperture Radar Data: Algorithms and Implementation*. Norwood, MA: Artech House, 2005.

[26] Y. Wang, H. Ling, and V. C. Chen, "ISAR motion compensation via adaptive joint time–frequency techniques," *IEEE Trans. Aerosp. Electron. Syst.*, vol. 34, no. 2, pp. 670–677, Apr. 1998.

[27] J. Wang and D. Kasilingam, "Global range alignment for ISAR," *IEEE Trans. Aerosp. Electron. Syst.*, vol. 39, no. 1, pp. 351–357, Jan. 2003.

[28] D. Zhu, L. Wang, Y. Yu, Q. Tao, and Z. Zhu, "Robust ISAR range alignment via minimizing the entropy of the average range profile," *IEEE Geosci. Remote Sens. Lett.*, vol. 6, no. 2, pp. 204–208, Apr. 2009.

[29] S. Li, Y. Xue, and L. Carin, "Bayesian compressive sensing," *IEEE Trans. Signal Process.*, vol. 56, no. 6, pp. 2346–2356, Jun. 2008.

[30] M. Grant, S. Boyd, and Y. Ye, cvx: Matlab Software for Disciplined Convex Programming. [Online]. Available: http://www.stanford.edu/~boyd/cvx/

[31] Y. Zhang, YALL1. [Online]. Available: http://www.caam.rice.edu/~optimization/L1/YALL1/

[32] H. Rohling, "Radar CFAR thresholding in clutter and multiple target situations," *IEEE Trans. Aerosp. Electron. Syst.*, vol. AES-19, no. 4, pp. 608–621, Jul. 1983.

[33] G. Davidson, Radar Toolbox. [Online]. Available: http://www.radarworks.com/software.htm

[34] C. R. Vogel and M. E. Oman, "Fast, robust total variation-based reconstruction of noisy, blurred images," *IEEE Trans. Image Process.*, vol. 7, no. 6, pp. 813–824, Jun. 1998.

[35] R. Acar and C. R. Vogel, "Analysis of bounded variation penalty methods for ill-posed problems," *Inverse Probl.*, vol. 10, pp. 1217–1229, 1994.

[36] C. R. Vogel, "Total variation regularization for ill-posed problems," Dept. Math. Sci., Montana State Univ., Bozeman, MT, Tech. Rep., Apr. 1993.

[37] S. P. Boyd and L. Vandenberghe, *Convex Optimization*. Cambridge, U.K.: Cambridge Univ. Press, 2004.

[38] O. Axelsson, *Iterative Solution Methods*. Cambridge, U.K.: Cambridge Univ. Press, 1994.

[39] W. Ye, T. S. Yeo, and Z. Bao, "Weighted least-squares estimation of phase errors for SAR/ISAR autofocus," *IEEE Trans. Geosci. Remote Sens.*, vol. 37, no. 5, pp. 2487–2494, Sep. 1999.

[40] D. E. Wahl, P. H. Eichel, D. C. Ghiglia, and C. V. Jakowatz, Jr., "Phase gradient autofocus—A robust tool for high resolution SAR phase correction," *IEEE Trans. Aerosp. Electron. Syst.*, vol. 30, no. 3, pp. 827–834, Jul. 1994.

[41] F. Berizzi and G. Cosini, "Autofocusing of inverse synthetic aperture radar images using contrast optimization," *IEEE Trans. Aerosp. Electron. Syst.*, vol. 32, no. 3, pp. 1185–1191, Jul. 1996.

[42] X. Li, G. S. Liu, and J. L. Ni, "Autofocusing of ISAR images based on entropy minimization," *IEEE Trans. Aerosp. Electron. Syst.*, vol. 35, no. 4, pp. 1240–1251, Oct. 1999.

[43] Y. Li, M. Xing, L. Zhang, and Z. Bao, "Detection, parameter estimation and imaging of maneuvering target in wide-band signal," *Sci. China Ser. F-Inf. Sci.*, vol. 52, no. 6, pp. 1015–1026, 2009.

[44] S. Zhu, G. Liao, Y. Qu, X. Liu, and Z. Zhou, "A new slant-range velocity ambiguity resolving approach of fast moving targets for SAR system," *IEEE Trans. Geosci. Remote Sens.*, vol. 48, no. 1, pp. 432–451, Jan. 2010.

[45] G. Y. Wang, X. G. Xia, and V. C. Chen, "Radar imaging of moving targets in foliage using multifrequency multiaperture polarimetric SAR," *IEEE Trans. Geosci. Remote Sens.*, vol. 41, no. 8, pp. 1755–1764, Aug. 2003.

[46] G. Wang, X. Xia, V. C. Chen, and R. L. Fiedler, "Detection, location, and imaging of fast moving targets using multifrequency antenna array SAR," *IEEE Trans. Aerosp. Electron. Syst.*, vol. 40, no. 1, pp. 345–354, Jan. 2004.

[47] R. Bose, A. Freeman, and B. D. Steinberg, "Sequence CLEAN: A modified deconvolution technique for microwave images of contiguous targets," *IEEE Trans. Aerosp. Electron. Syst.*, vol. 38, no. 1, pp. 89–96, Jan. 2002.

Lei Zhang was born in Zhejiang Province, China, in 1984. He received the B.S. degree in mechanism and electrical engineering from Chang'an University, Xi'an, China, in 2006. He is currently working toward Ph.D. degree in signal processing in the National Key Laboratory of Radar Signal Processing, Xidian University, Xi'an.

His major research interests are radar imaging (synthetic aperture radar (SAR)/inverse SAR).

Zhi-jun Qiao (M'10) received the Ph.D. degree in applied mathematics from the Institute of Mathematics, Fudan University, Shanghai, China, in 1997, wherein his dissertation was one of the first 100 excellent Ph.D. dissertations awarded in 1999.

From 1999 to 2001, he was a Humboldt Research Fellow with the Department of Mathematics and Computer Science, University of Kassel, Kassel, Germany. From 2001 to 2004, he was a Researcher with the Theoretical Division, Los Alamos National Laboratory. In 1997, he became a Professor with the Department of Mathematics, Liaoning University, Shenyang City, China. Currently, he is the PI of two grants under the Department of Defense Program and the Norman Hackerman Advanced Research Program. He is currently with the Department of Mathematics, The University of Texas-Pan American, Edinburg, TX. He is currently the Editor-in-Chief of the *Pacific Journal of Applied Mathematics*. He has published two monographs and more than 90 articles in peer-reviewed international journals. His research interest includes nonlinear partial differential equations and its application in radar imaging.

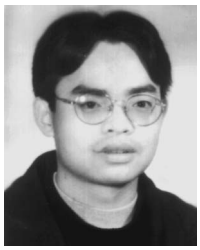

Mengdao Xing (M'04) was born in Zhejiang, China, in November 1975. He received the B.S. and Ph.D. degrees in electrical engineering from Xidian University, Xi'an, China, in 1997 and 2002, respectively.

He is currently a Full Professor with the National Key Laboratory of Radar Signal Processing, Xidian University. His research interests include synthetic aperture radar (SAR), inverse SAR, and over-the-horizon radar.

Yachao Li was born in Jiangxi Province, China, in 1982. He received the Ph.D. degree from Xidian University, Xi'an, China, in 2008.

Currently, he is an Associate Professor with the National Key Laboratory of Radar Signal Processing, Xidian University. His research interests are radar imaging and ground moving-target indication.

Zheng Bao (M'80–SM'90) was born in Jiangsu, China. He received the B.S degree in radar engineering from Xidian University, Xi'an, China, in 1953.

Currently, he is a Professor with Xidian University, Xi'an, China, where he is also the Chairman of the academic board of the National Key Laboratory of Radar Signal Processing. He has authored or coauthored 6 books and published over 300 papers. Currently, his research fields include space-time adaptive processing, radar imaging (synthetic aperture radar (SAR)/inverse SAR), automatic target recognition, and over-the-horizon radar signal processing.

Prof. Bao is a member of the Chinese Academy of Sciences.